UNIVERSITY OF GRONINGEN

BACHELOR RESEARCH PROJECT

Kinetic *In Situ* Single-Layer Synthesis Bulk Holder Optimization & Graphene KISS Exfoliation Exploration in Ambient and UHV Environment

Author
Jouke de Boer

Supervisor & First Examiner
Dr. Antonija Grubišić-Čabo

Second Examiner
Prof. Dr. Ir. Ronnie Hoekstra

July 7, 2024

ABSTRACT

*T*HIS *research introduces a novel design of a kinetic in situ single-layer synthesis bulk holders to improve exfoliation efficacy, using FreeCAD. The designs replace a double washer mechanism with a solid piece of metal, improving holder strength. In addition to eliminating bolt threads that hinder motion. A mechanism with pins to restrict rotation is also introduced. Potentially leading to more consistent exfoliation results. Furthermore, the efficacy of graphene KISS exfoliation was assessed under both ambient conditions using flame-annealed Au(111)/mica as the substrate, and in ultra-high vacuum using radiation-annealed and sputtered Au(111)/mica. Optical microscopy and low-energy electron diffraction was used to measure the size and quality of the crystals exfoliated. The first method yielded four multilayered graphene crystals with measured lengths spanning 10.30 - 173.13 µm, depending on angle measured. With crystal areas in the range of 413.15 - 5273.03 µm^2. The second method produced large groups of smaller multilayered crystals with areas in the range of 4459.09 - 8125.51 µm^2. In addition to yielding a thin region of multilayered graphene crystals with a measured length of 135.42 µm. Using ultra-high vacuum resulted in a sample with less contamination, and qualitative low-energy electron diffraction characterization determined the relative angle of the graphene crystal exfoliated with respect to the Au(111)/mica to be 31.5°. Ultimately, crystal size alone is an insufficient metric to determine and compare exfoliation effectiveness, since both methods produced crystals with variations in quality, quantity, thickness, and shape. Additionally, the limited number of attempts was insufficient for a conclusive efficacy assessment, and further research with statistically significant data is required.*

Contents

I Introduction

THE interest in two-dimensional materials started in the early 2000s, when exfoliation using mechanical peeling with tape was used to manufacture graphene. The discovery of graphene, a single layer of graphite, was honored with the 2010 Nobel Prize in Physics to Andre Geim and Konstantin Novoselov, highlighting the significance of research regarding 2D materials.[1,2]

Graphene boasts a remarkable combination of properties, including exceptional electrical conductivity, mechanical strength, and a large surface area.[3–5] These characteristics have opened doors to a vast array of potential applications across various fields. The use of graphene in the anode of a lithium-ion battery significantly improves its performance.[6] Moreover, the lifetime of silicon-based high capacity batteries can be significantly increased by coating the anodes of the batteries with graphene, this increased resistance to mechanical stress induced by the charge and discharge cycles.[7] Finally, graphene's remarkable electron mobility allowed for creation of faster field-effect transistors with significantly faster processing speed.[8]

However, not all material can be thinned down easily into 2D crystals. Brittle crystals like hexagonal boron nitrite have been shown to be rather difficult to exfoliate, resulting in small crystals whose properties are hard to analyze. Moreover, inherent limitations in yield, adhesion, and contamination have showed a need for alternative approaches and improvements in current methods. The kinetic *in situ* single-layer synthesis (KISS) method, is a promising method that offers a pathway to surmount these challenges.[9] This method uses gold substrates as an exfoliation tape and is done in ultra-high vacuum (UHV), thus minimizing contamination. In addition to resorting to exceptionally flat clean substrates, improving adhesion to the substrate.

Motivated by the potential of the KISS method, this research aims to make the process even more effective and user-friendly, by designing an improved bulk holder in FreeCAD. With changes in design focused on improving strength, user-friendliness, and a smooth consistent compressive and decompressive motion, resulting in the more reliable and faster production of larger higher quality crystals. Additionally, graphene will be produced using the KISS method in ultra-high vacuum using a radiation-annealed and sputtered Au(111)/mica substrate, and under ambient conditions using a flame-annealed Au(111)/mica substrate and the KISS method of exfoliation. Optical microscopy will be used to analyze the results and measure the size of the exfoliated crystals. Low-energy electron diffraction will be used to analyze the success of the exfoliation.

Upon data acquisition and analysis, a definitive answer can be reached regarding the question: *How should the bulk holder be adjusted to improve user-friendliness, strength, and effectiveness of exfoliation, and how effective is graphene UHV KISS exfoliation on ion sputtered and annealed Au(111)/mica, and how does it compare to its ambient flame-annealed counterpart?*

II Theory

I Applications of 2D Materials

RESEARCH regarding 2D materials increased when graphene, a single layer of graphite, showed outstanding physical properties that it does not exhibit when viewing its bulk counterpart. This prompted other materials to be researched extensively to determine new properties when the material is created in its two-dimensional form. The most important properties are shown in *Table 1*. Practical applications of graphene are already leading to significant advancements related to battery lifetime improvements, increased transistor speed, more accurate photodetectors, and improved drug delivery in the human body.

The incorporation of graphene into lithium-ion batteries presents a promising path for significant advancements in their performance. By doping graphene anodes with electronegative ions, the electrochemical battery performance can be significantly improved.[6] The high surface area allows for an improved connection between the electrolyte and the electrode, leading to improved power handling capabilities, which translates to faster charging and discharging rates, crucial for applications demanding rapid energy delivery and storage. The lower weight of graphene compared to traditional materials offers an additional benefit, contributing to a higher energy density for the entire battery system. Graphene offers a solution to the challenge of limited cycle life experienced with high-capacity batteries with silicon-based anodes. Silicon's superior capacity for storing lithium ions comes at the cost of significant mechanical stress during charging and discharging cycles. This stress causes the silicon to swell and contract repeatedly, leading to

electrode degradation. Graphene's properties can be leveraged to mitigate this issue. By incorporating graphene into the anode structure, a conductive and structurally rigid network is formed. This network acts as scaffolding, effectively accommodating the volume changes of the silicon during cycling and preventing its deterioration. The result is a longer cycle life for the battery, extending its overall lifespan.[7] The potential applications of graphene extend beyond conventional rigid battery formats. The use of graphene as a current collector lays the foundation for the development of truly flexible batteries.[10] Graphene's inherent flexibility, combined with its lightweight nature, opens doors for the creation of batteries that can be seamlessly integrated into fabrics. Such advancements hold immense promise for wearable electronics and other applications requiring lightweight and conformable energy storage solutions.

Table 1: Properties of graphene.[11]

Physicochemical Property	Estimated Value[3–5,12]
High Surface Area to Weight Ratio	$\sim 2630\,\mathrm{m^2 g^{-1}}$
Excellent Electrical Conductivity	$\sim 1738\,\mathrm{siemens\,m^{-1}}$
Strong mechanical strength	Young's Modulus $\sim 1100\,\mathrm{GPa}$
	Fracture Strength $\sim 125\,\mathrm{GPa}$
Thermal Conductivity	$\sim 5000\,\mathrm{Wm^{-1}K^{-1}}$
Ease of Functionalization	Electrostatic Interaction
	π-π Stacking Interaction

On the other hand, graphene's remarkable electron mobility allowed for creation of faster field-effect transistors, lowering processing times in integrated circuits.[8] This was facilitated using graphene nanoribbons (GNRs). The design shown in *Figure 1*, consists of armchair graphene nanowire (AGNR) with a 10 nm long intrinsic channel placed between two insulator layers of silicon dioxide. Heavily GNR doped source and drain regions are located on either end of the intrinsic GNR channel. Field-effect transistors utilize an electric field generated by a voltage on the gate terminal to modulate the conductivity between the source and drain terminals in a semiconductor, enabling control of current flow without a significant input current. A positive V_{gs} and V_{ds} are used in this setup for current to flow to occur, increasing either one increases current flow through the system.
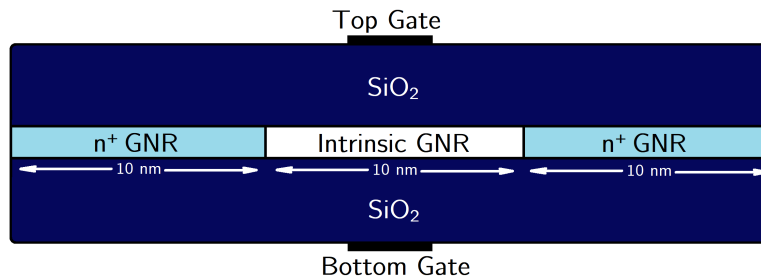

Figure 1: Schematic diagram of a DG-GNRFET.[8]

Moreover, due to the high surface area, phenomenal electrical conductivity, and capability to adsorb a variety of biomolecules, graphene has been considered as an ideal transducing material for the construction of electrochemical biosensors. Graphene boasts a large surface area which allows for more molecules to interact with the sensor, and its exceptional electrical conductivity improves the transferring of the signal generated by these interactions. The efficacy of electrochemical sensors hinges on the distance between the electrode's surface and the target molecule's site. In graphene, electron transfer typically occurs at its edges or at basal plane defects, making it ever more important that the 2D structure of graphene has a large surface area, increasing places where targeted biosensing interactions can occur, and lowering the distance between the target molecules and graphene.

Furthermore, the specific edge structure named zigzag or armchair (ZGNR or AGNR) determine specific physical properties, ZGNR exhibiting metallic behavior while AGNR can potentially semiconduct, both shown in *Figure 2*. Making ZGNR an attractive alternative to copper for interconnects in integrated circuits using its metallic properties, and AGNR viable in devices like solar cells, laser diodes, and image sensors utilizing the semiconducting variant of the material.[13]

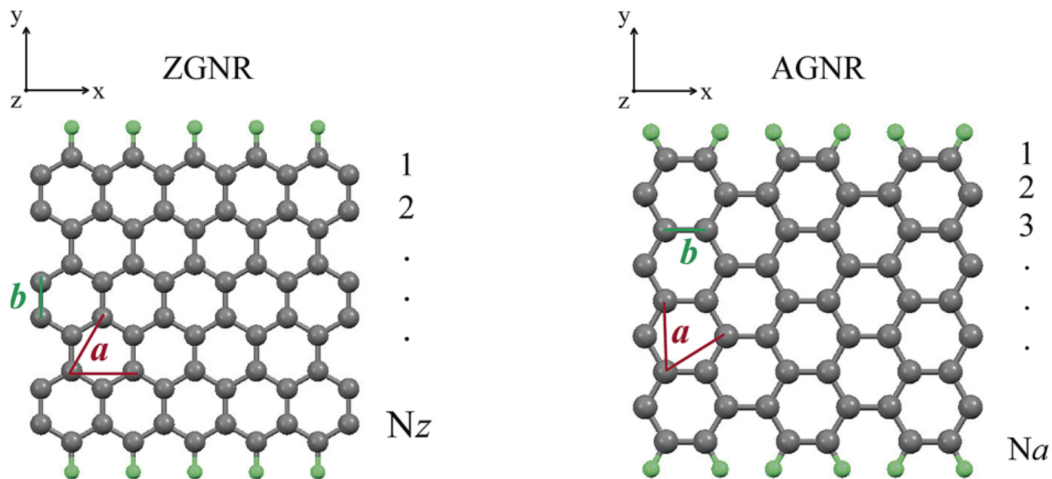university of groningen   faculty of science and engineering

Figure 2: Two edge structures of graphene.[13]

Additionally, graphene is known to be highly reliable in capturing aromatic molecules, a ring of atoms in a molecule with alternating single and double bonds that exhibits stability due to electron delocalization, through π-π stacking. The aromaticity of graphene is centralized within the set of hexagonal rings, with two π-electrons delocalized over every hexagonal ring of the aromatic graphene structure. The stacked structures are held together by the favorable positions of the electron clouds of both structures, although no covalent bonds occur, weak electrostatic and van der Waals attraction do take place between one another. *Figure 3* shows possible stacking orientations. The choice of interaction depends on the specific target molecule and desired outcome. Organic molecules typically interact with graphene via van der Waals forces. Pristine graphene lacks oxygen atoms, so ionic interactions are not possible due to the hybridized sp^2 orbitals of the carbon atoms being planar. While graphene oxides can engage in ionic interactions and bond with other molecules, as a result of newly formed sp^3 hybridized orbitals.

π-π stacking occurs when π orbitals of two rather big non-polar aromatic rings overlap. These bonds are as strong as covalent bonds but compared to them, no conjugations of graphene sheets are disrupted, thus the electronic properties of graphene are saved. Similar interactions can occur even when the rings are arranged in T-shaped arrangements, also shown in *Figure 3*. Notably, these interactions play a crucial role in electrochemical, fluorescence, and optical biosensing by π-stacking with DNA and RNA base pairs.
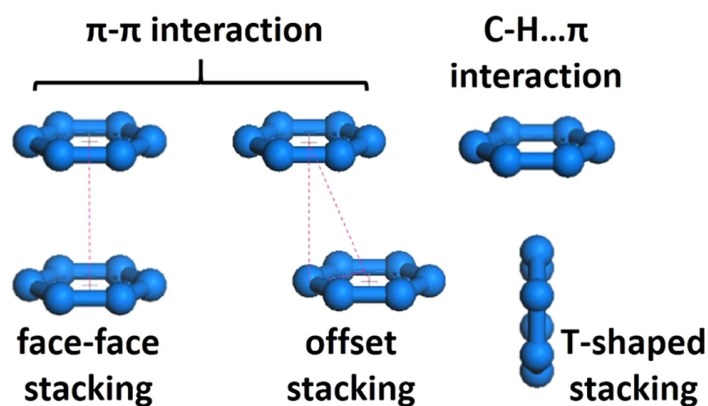

Figure 3: Graphene stacking orientation and positions on an aromatic ring.[14]

A key advantage of these non-covalent interactions is that they do not disrupt the lattice structure of graphene. This ensures that crucial properties like electrical conductivity, mechanical strength, and solubility remain intact. For larger systems like polymers with repeating aromatic rings, multiple π-π interactions can lead to strong binding, creating highly homogeneous composites with improved mechanical, electrical, and thermal properties. Conversely, the weaker interactions with smaller molecules make them easier to attach and detach, a valuable feature for applications like drug delivery systems where controlled release is desired.

Furthermore, creating quantum dots using graphene showed potential in improving the classical silicon nanowire (SiNW) based photodetectors. Unlike traditional quantum dots, which contain heavy metals, GQDs are made from carbon and exhibit lower toxicity. This makes them more biocompatible and opens doors for potential applications in biomedicine. Secondly, the GQDs showed promise in improving the yellow photoluminescence emission along with large band gap formation and the introduction of new states within the band gap, when creating a heterostructure that uses poly(ethyleneimine)-functionalized graphene quantum dots (GQD$^{\mathrm{PEI}}$s) combined with the traditional SiNW a photodetector can be made with improved specifications.[15]

This GQD$^{\mathrm{PEI}}$/SiNW photodetector exhibited a remarkable improvement of the photocurrent to dark current ratio ($I_{\mathrm{ph}}/I_{\mathrm{dark}}$), which quantifies the ability of the device to distinguish the photocurrent I_{ph} generated by light from the inherent dark current I_{dark} present even in the absence of illumination. A high $I_{\mathrm{ph}}/I_{\mathrm{dark}}$, in this case 90, signifies sensitivity allowing for the detection of weak light signals. It improves the signal-to-noise ratio leading to clearer and more reliable information. Furthermore, a high $I_{\mathrm{ph}}/I_{\mathrm{dark}}$ expands the detector's dynamic range, enabling it to function effectively across a broader spectrum of light intensities. Consequently, a high $I_{\mathrm{ph}}/I_{\mathrm{dark}}$ is paramount in developing high-performance photodetectors.

(a) Reference photodetector, experiencing darkness.   *(b) Reference photodetector, illuminated.*   *(c) GQD^{PEI} enhanced heterojunction, experiencing darkness.*   *(d) GQD^{PEI} enhanced heterojunction, illuminated.*
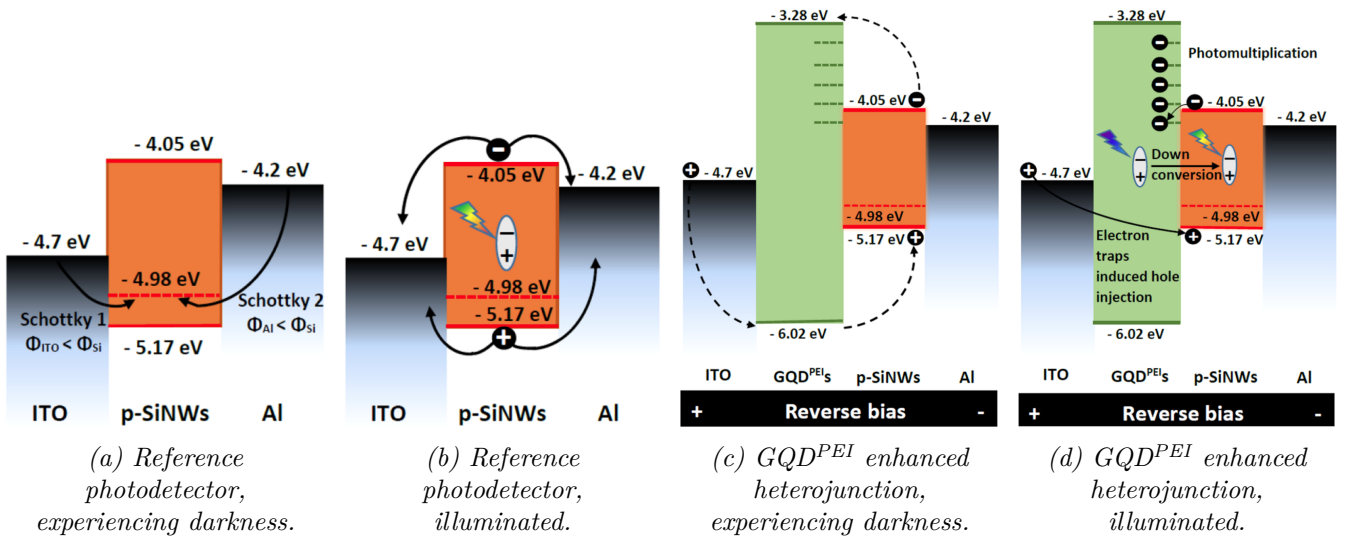
Figure 4: Energy band diagrams of SiNW photodetectors, under varying illumination conditions.[15]

To illustrate the cause for the discussed improvement in functionality using GQD$^{\mathrm{PEI}}$, energy band diagrams of various photodetectors are depicted in *Figure 4*, where *Figure 4a* shows the structure lacking a quantum dot layer experiencing darkness. In this case, electrons move from the metal to the p-type semiconductor caused the work function difference between the electrodes and p-type silicon, resembling the behavior of two Schottky diodes connected back-to-back. When the reference photodetector is illuminated, *Figure 4b*, an electron hole pair is generated. A slight increases photocurrent occurs as carriers recombine at the electrodes.

The GQD$^{\mathrm{PEI}}$/SiNW heterostructure shown in *Figure 4c* shows the quantum dot band gap encompassing silicon's, creating a type I heterojunction with a substantial barrier at the interface. In the dark, a type I heterostructure in a photodetector helps minimize dark current, this unwanted current. The built-in barrier, hindering thermally excited electrons from reaching the opposite electrode and contributing to dark current. This translates to a cleaner signal when light actually hits the detector. *Figure 4d* depicts the GQD$^{\mathrm{PEI}}$/SiNW heterostructure under illumination, when thin enough, light generates electron-hole pairs in both SiNW and GQD$^{\mathrm{PEI}}$. The built-in electric field separates these charges, with electrons sweep by the GQD$^{\mathrm{PEI}}$ side toward the front contact, and the holes cross the silicon towards the back contact. Electron transport is slightly limited by the energy level offset of the GQD$^{\mathrm{PEI}}$/SiNW heterostructure. However, the presence of specific energy levels within the GQD$^{\mathrm{PEI}}$ tarp electrons when the device is illuminated. The ability of GQD$^{\mathrm{PEI}}$ to trap electrons under light exposure triggers a beneficial effect, it causes a reduction in the energy barrier for holes to enter the material. This consequently allows for more secondary charge carriers to be injected when a reverse bias is applied, ultimately enhancing the device's external quantum efficiency, which indicates what fraction of incoming photons are used to cre-

university of groningen   faculty of science and engineering

ate electricity. At high light intensities, all the available traps become filled with electrons, limiting their effectiveness. Additionally, the presence of intermediate energy levels within GQD^{PEI} offer a temporary reservoir for electrons, extending their lifespan within the device. This prevents electrons and holes from recombining prematurely, which would otherwise hinder efficiency. There is a trade-off to consider regarding the thickness of the GQD^{PEI} layer. While it does offer the aforementioned benefits, a very thick layer can start to block incoming light. This significantly reduces the amount of light reaching the device and leads to lower performance, especially when more than six layers of quantum dots are deposited on the silicon nanowire substrate.

Two-dimensional material research since the discovery of graphene points towards a future filled with improved electronics in various fields. Graphene exhibits a range of properties that make it suitable for various applications. These include its high surface area, excellent electrical conductivity, strong mechanical strength. Graphene was used to improve battery performance, create faster transistors, and develop more sensitive biosensors. Lastly, the use of graphene in quantum dots has shown promise in enhancing photodetectors, indicating the future of research regarding 2D material is bright.
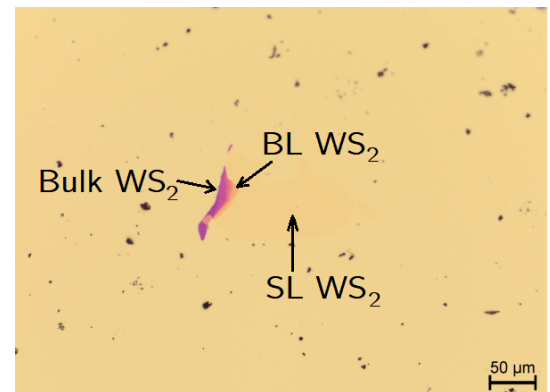
II   Surface Structure Determination

SURFACES structures can be analyzed in various ways, this is done to determine the size and quality of the crystal exfoliated. Large area single-layered graphene is desired, exfoliation can also result in bi-layered or multilayered structures, although an increase in the quantity of crystal layers does affect the properties of the material exfoliated. Areas with large amount of crystal layers are considered bulk material, these are not desired. This subchapter describes various techniques to analyze a material's structure. While optical microscopes use visible light and lenses for a magnified view, low-energy electron diffraction uses an electron beam to analyze the surface. Each technique provides complementary information about the material's structure due to its unique way of capturing information.

Optical microscopes offer a noninvasive way to determine the form, shape, structure, and size of the flakes exfoliated on the surface. Although the information gathered using this technique is still limited, it does give a large a amount of information about the size and location of the crystals exfoliated on the substrate. An image of example results are shown in *Figure 5*, to illustrate the information that can be gathered using am optical microscope. Although an optical microscope does not have a relatively high resolution, the magnification is significant enough to show single, double and bulk layers of MoS_2. Showing the importance of the use of these types of microscope regarding this field.

Figure 5: Example result using an optical microscope with SL, BL, and bulk $WS_2/Au(111)$.[9]

While the term microscope often refers to compound microscopes, there is a simpler design known as a single microscope. This microscope uses a single convex lens to magnify an object. It offers a low magnification power, typically ranging from 5x to 30x. Due to this limitation, single microscopes are not suited for the magnification of particles with only tens of nanometers in size. Compound microscopes use a series of lenses to achieve much higher magnifications. These microscopes use an objective lens close to the sample and an eyepiece lens for viewing. By passing light through the sample and then these two lenses, they allow for a detailed examination of much smaller objects up to with a resolution as low as $0.2\,\mu m$ when using visible light,[16] as a result of the Rayleigh criterion which the generally accepted criterion for the minimum resolvable detail. Lastly, digital microscopes combine traditional microscopy with digital cameras, offering on-screen visuals, image manipulation, and measurement tools. Although their magnification may not reach the magnification of a high-end compound microscope, which is the microscope used to analyze the exfoliation results gathered.

Low-energy electron diffraction (LEED) can be used for qualitative pattern and quantitative structure determination. It works by firing a beam of low-energy electron at the sample surface, these electrons typically have a kinetic energy of 30-200 eV. LEED instruments are always found within vacuum chambers, since the electron filament inside cannot operate in a pressure higher than 5^{-8} mbar. The filament will

burn out if it is used in when the pressure is too high, and the mean free path of the electrons also decreases as pressure rises, making the electrons eventually unable to reach the detectors.

A schematic overview of the LEED detectors is shown in *Figure 6*, consisting of an electron gun and four metal grids. The first grid is grounded to create a field-free region around the sample, allowing for unobstructed interaction with the electrons. The next two grids are set to a specific retarding voltage, this voltage acts as a filter, repelling most inelastically scattered electrons, those that have lost energy due to collisions within the solid. Only elastically scattered electrons, which retain most of their initial energy after interacting with the atomic lattice of the sample, are able to pass through these retarding grids. The remaining electrons then travel through another grounded grid before being accelerated towards a positively charged fluorescent screen. The emitted light forms the characteristic LEED pattern, which can be observed through a viewport in the vacuum chamber or captured with a camera for further analysis.

Figure 6: LEED schematic.[17]

Generally, interactions happen between incoming electrons and the outermost layer of atoms. However, higher energy electrons can penetrate deeper, interacting with atoms in underlying layers as well. The diffracted electrons are then captured on a fluorescent screen, forming a specific pattern of bright spots, which show a reciprocal space representation of the lattice structured measured. Au(111)/mica and graphene both show a hexagonally shaped pattern when qualitatively measured with LEED. Since LEED shows the crystal structure representation in reciprocal space, when these structures are small in real space they become large in the reciprocal space. The inverse is true for lattice structures that are large in real space, meaning graphene will show a larger hexagonal LEED pattern than Au(111)/mica, because graphene's crystal structure is smaller in real space.

LEED can be used in two ways. Qualitatively, where the diffraction pattern is created by the electrons and analyze the positions of the spots in the pattern. This analysis provides information about the symmetry of the surface being studied. If there are atoms or molecules adsorbed on the surface, the qualitative analysis can also reveal clues about their size and how they are oriented relative to the underlying surface. Additionally, LEED can also be used quantitatively. In this case, the intensity of the diffracted electrons are measured as a function of electron intensity of the electron beam used. This data is then plotted as a curve, which is compared to theoretical models. By comparing the measured intensity curves to those predicted by theoretical models for different atomic arrangements, the positions of the atoms on the surface can be determined. In turn, giving information about the crystal structures of the materials used, making it possible to determine the positions and orientation of both structures. This research uses LEED purely qualitatively, to determine the success of exfoliation.

Figure 7: Schematic shows how LEED imaging is displayed at the viewpoint.[17]

The impact the angle of emission has on the qualitative pattern shown on the viewpoint is schematically depicted in *Figure 7*. An important relation to note is the relation between the distance from the center d_{hk}, and the magnitude of the scattered electrons' wave vector $\mathbf{k}_s$. Firstly, $\mathbf{k}_s$ can be used to determine emission angle of a beam $\sin(\Theta_{hk}) = |\mathbf{g}|/|\mathbf{k}_s|$, with reciprocal lattice vector $\mathbf{g} = h\mathbf{b}_1 + k\mathbf{b}_2$. Secondly, with this information the distance from the center of the viewpoint can be determined using *Equation 1*. This shows that increasing the electron energy decreases the distance from the center of the viewpoint, making space for new spots to move in from the sides.

$$d_{hk} = R\sin(\Theta_{hk}) = \frac{R}{|\mathbf{K}_s|}|h\mathbf{b}_1 + k\mathbf{b}_2| = R\frac{\hbar}{\sqrt{2m_e}}\frac{1}{\sqrt{E}}|h\mathbf{b}_1 + k\mathbf{b}_2| \qquad (1)$$
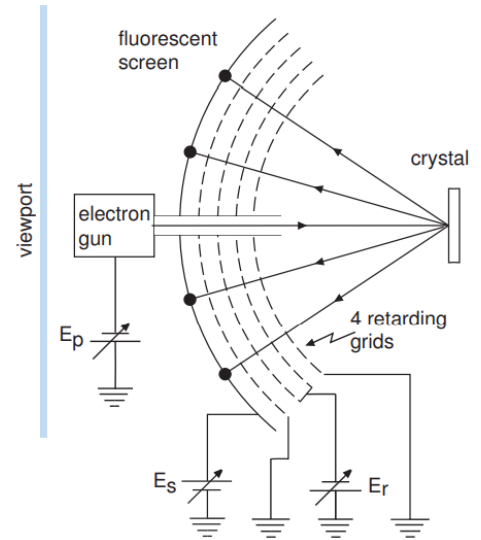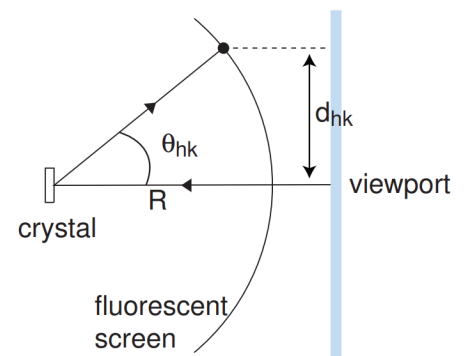
Analysis of quantitative and qualitative patterns measured can be done by with the assumption of a purely 2D material, although the discussion of diffraction from a two-dimensional lattice is quite similar to that of a bulk material. With the diffraction conditions for a two-dimensional lattice are given by the Laue condition given by *Equation 2*.

$$(\mathbf{k}_s^{\parallel} - \mathbf{k}_i^{\parallel}) = \mathbf{\Delta k} = \mathbf{g} \tag{2}$$

Here, $\mathbf{k}_s^{\parallel}$ and $\mathbf{k}_i^{\parallel}$ represent the wave vectors of the scattered and incident radiation parallel to the surface. The wave vector captures both the direction and intensity of the wave's propagation. $\mathbf{\Delta k}$ represents the change in the wave vector due to the scattering interaction with the lattice. Finally, $\mathbf{g}$ stands for a reciprocal lattice vector. In essence, the Laue conditions state that for a strong diffracted beam to be observed, the change in the wave vector caused by the scattering needs to be exactly equal to a reciprocal lattice vector. Note that the incident and scattering wave vectors perpendicular to the surface are disregarded, because the surface lattice is only two-dimensional. There is one condition for the vertical components, because the conservation of momentum $|\mathbf{k}_s| = |\mathbf{k}_i|$ needs to hold, which is a requirement of elastic scattering.

To visualize how and when waves interact with crystal structure, the Ewald construction can be used. It involves using the reciprocal lattice space as well as drawing a circle of radius $|\mathbf{k}_i|$. For the surface case, there is no Laue condition perpendicular to the surface, and this is taken into account by replacing the discrete points in the Ewald by rods perpendicular to the surface. This can be justified by arguing that the points perpendicular to the surface in real-space have infinite periodicity, meaning that the reciprocal lattice points are infinity close to each other, forming the rods.
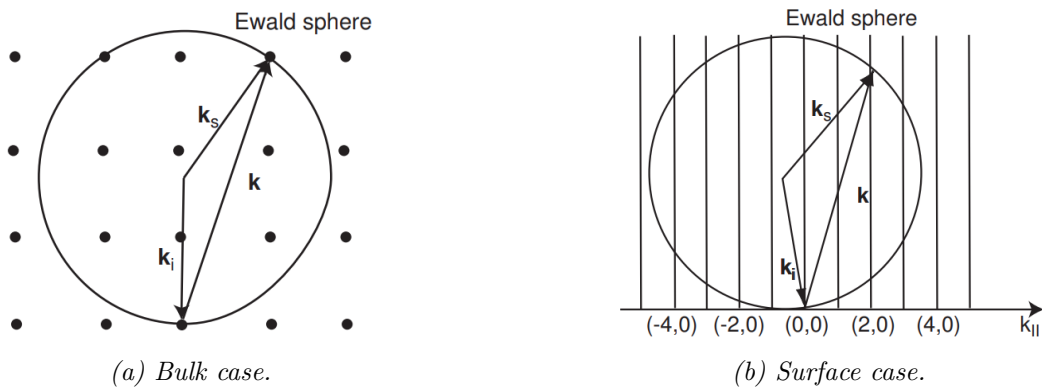

(a) Bulk case.   *(b) Surface case.*

Figure 8: Two cases of the construction of the Ewald sphere.[17]

Constructive interference is expected at the intersections of the rods and the sphere, which happens more often when electron energy is increased. More points are also expected in the two-dimensional case, since the sphere only has to intersect the rods, and does not necessary need to hit points in k-space. In most cases, the incident radiation parallel to the surface is very close to zero, meaning $\mathbf{k}_i^{\parallel} = 0$. When this is the case, *Equation 2* can then be used to show that $\mathbf{k}_s^{\parallel} = \mathbf{g}$, implying that the diffraction pattern directly shows the surface reciprocal lattice.
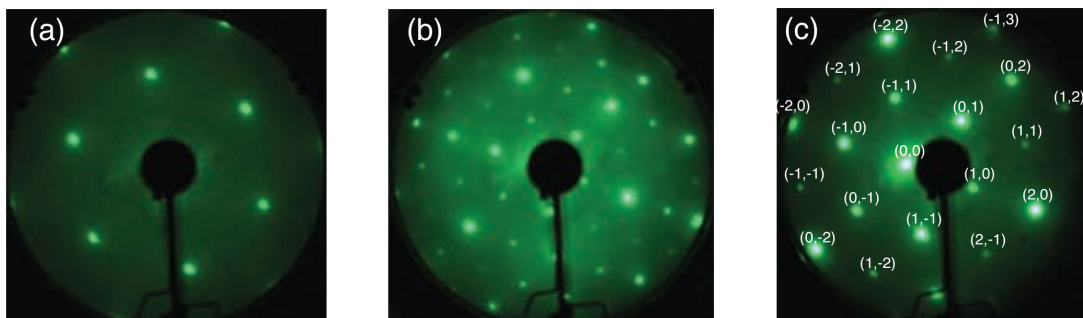

Figure 9: LEED example results of an FCC(111) two-dimensional structure, with (a) low energy (77 eV), (b) high energy (330 eV), and (c) off-normal making (0,0) visible.[17]

The spots making up the pattern shown are affected by arrangements of crystals with respect to each other, slight rotational misalignment of crystals inside a polycrystalline structure can cause spots to appear wider. The LEED pattern is indexed according to the reciprocal lattice of the bulk-terminated surface. This means that additional spots, like the (1/2,0) in the case of a reconstructed surface, will appear due to the altered periodicity. The (0,0) spot, corresponding to the directly transmitted beam, is usually absent in normal-incidence LEED due to the electron gun blocking it. Although *Figure 8* would suggest that all diffraction spots have similar intensities as electron energy is varied, this is in practice not the case. This is mainly caused by the electrons actually penetrating the solid relative to electron energy, increasing energy increases their depth. Giving rise to a third Laue condition $\mathbf{k}_s^\perp - \mathbf{k}_i^\perp = \mathbf{g}^\perp$.
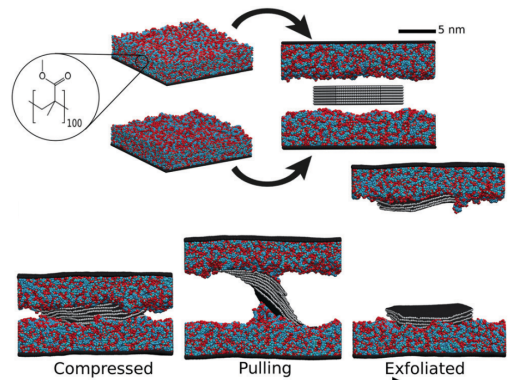
Lastly, quantitative LEED analysis encounters an observed intensity maxima that is at a lower kinetic energy than the calculated maxima. Caused by electrons experiencing an inner potential inside the solid. Leading to a shift in the diffraction maxima towards lower measured kinetic energies compared to the calculated values. Additionally, the inner potential bends the electron trajectory, causing peak broadening and influencing the sharpness of the pattern. This broadening comes from the limited penetration depth of electrons, which creates uncertainty in their momentum and energy. Overall,

III   Exfoliation Methods & Advancements

EXFOLIATION refers to the process of separating thin layers from a bulk material. In physics, this phenomenon is often studied in the context of layered materials, where weak interlayer forces hold individual sheets together compared to the strong bond between substrate and exfoliant. This disparity in bonding strength allows for the application of external forces to overcome the weak interlayer interactions, effectively peeling off individual layers. The specific mechanism of exfoliation can vary depending on the material and the applied technique.

Micromechanical cleaving of graphite using sticky tape was the first method of exfoliation, this method can be considered imprecise and labor-intensive. Mechanical exfoliation of graphene can be achieved through two primary mechanisms, mode I and mode II fracture. Mode I fracture is achieved by applying a force perpendicular to the graphene plane. whereas mode II fracture involves a shearing force applied laterally across the surface of the graphene. The effectiveness of two mechanical fracturing methods on a material can be investigated through computational simulations. A simulated polymer tape model can be used to represent the material and analyze the efficacy of each method.[18] This simulation provides atomic-scale understanding of a process widely employed in laboratories, where Scotch tape is used for mechanical exfoliation. A realistic in-silico model can be constructed, mimicking a graphite stack positioned between two polymer layers. Poly-methylmethacrylate (PMMA) and poly-dimethyl-siloxane (PDMS) were chosen as the polymers to represent the pressure-

Figure 10: 88 poly(100)methylmethacrylate slabs used when sticky tape exfoliating seven layers of 120 nm graphene flakes.[18]

sensitive adhesive properties characteristic of tapes, shown in *Figure 10*. The simulation mimicked the tape application process by compressing the system along the xy-axis. Subsequently, the simulation box was subjected to tensile strain, replicating the peeling motion of the tape. The stress response along the peeling direction was monitored to identify the point of exfoliation, characterized by a drop in stress to zero. The polymer chains used consisted of 100 monomer units which is below the commercial sticky tape polymer length, but above the entanglement length. To make sure that the adhesive properties are retained, since the entanglement length refers to the critical length a polymer chain needs to reach before it gets significantly restricted in its movement by interactions with other polymer chains.

Despite the chaotic nature of the simulations, the effectiveness of certain starting parameters for graphene exfoliation using polymer tapes can still be determined. A variable that did not have significant effect on the flake quality was the strain rate. Lateral dimension, also known as box size, could be doubled to show a higher average layer exfoliation and significantly lower energy needed to remove an atom of material. Furthermore, the used techniques named OPLS and GraFF are force field strategies. OPLS is

a well-established simulation technique that recreates the interactions between polymer molecules. For the graphene and graphite GraFF can be used, this is a force field adept at modeling interactions within carbonaceous materials. By incorporating GraFF, the strong covalent bonds holding the graphene flakes together and influencing their interactions with the polymer tape can be simulated. Only using OPLS causes no exfoliation to occur showing that GraFF is necessary to facilitate and simulate exfoliation. The specific impact of the adjustments to certain parameters is displayed in *Table 2*.

Table 2: Graphite exfoliation simulation results varying certain initial conditions.[18]

Simulation Label	1	2	3	4	5	6
Force Field		OPLS	&	GraFF		OPLS
Pull Speed (ms^{-1})	1	10	10	10	10	10
Box Size (nm)	100	100	200	200	200	200
Flake Diameter (nm)	60	60	60	120	120	120
Polymer Type	PMMA	PMMA	PMMA	PMMA	PDMS	PMMA
Energy to Remove per Atom (meV)	12.0	13.3	7.46	13.7	13.2	n/a
Nr. Replicas in Ensable	5	50	10	15	14	10
Average Exfoliated Layers	0.8	1.66	2.0	0.87	2.4	0
0 Layers Exfoliated	1	4	1	5	1	10
1 Layer Exfoliated	3	17	3	8	1	0
2 Layers Exfoliated	1	21	1	1	3	0
3 Layers Exfoliated	0	8	5	1	9	0

When it comes to mechanically exfoliating graphene, the choice of polymer used to peel the layers apart significantly impacts the process. Two popular options are PMMA (polymethyl methacrylate) and PDMS (polydimethylsiloxane), and they work in fundamentally different ways. Due to its higher viscosity, PMMA offers a controlled touch. PMMA bends and slides along the graphene layers, minimizing the energy required for separation. This approach is advantageous because it tends to produce single layers of graphene more reliably. On the other hand, PDMS, being less viscous, interacts with graphene through a "shearing mechanism". PDMS tends to adhere to multiple layers at once while also being

Figure 11: Effect of polymer type on the amount of graphene sheets exfoliated.[18]

able to mold around the graphite, making it less likely to achieve single-layer graphene. This increased contact actually discourages the separation of individual layers and instead favors breaking the graphite in the middle.The Importance of viscosity and timescales.
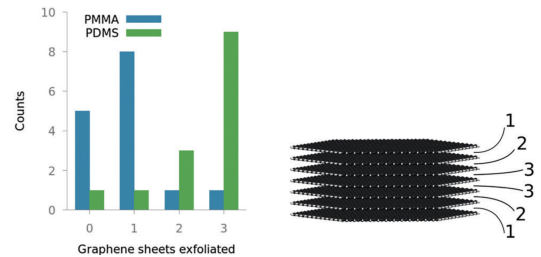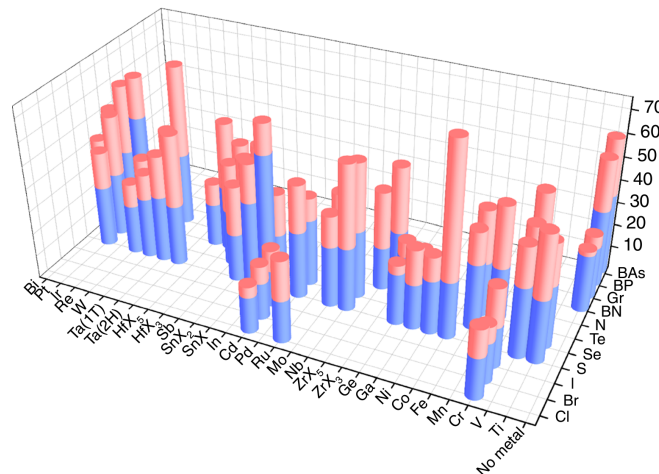

Figure 12: Bar graph of interlayer binding energy (blue), and adsorption energies on Au(111) (red). Where the visible red cylinders show the difference of the two energies.[19]

The key difference between PMMA and PDMS lies in their viscosity. PMMA's higher viscosity allows for a more controlled peeling process, while PDMS's fluidity promotes shearing. Interestingly, these properties are dynamic, meaning that the speed and duration of the exfoliation process can influence the outcome. For instance, using a shorter dwell time with PDMS might limit its ability to mold around the graphite, potentially favoring single-layer graphene production. The ideal polymer for graphene exfoliation based on these observations, research suggest that higher viscosity polymers are better suited for graphene exfoliation. Additionally, cross-linking PDMS, which essentially stiffens its structure, could further improve its performance in achieving single-layer graphene.

To determine if a material is suitable for exfoliation a comparison can be made between the interlayer binding energy of the exfoliation material and the adsorption energy of the substrate material. An example of this done is shown in *Figure 12*, where gold is used as the substrate and exfoliation material. The results overwhelmingly demonstrate that the 2D crystal/Au interaction is consistently stronger than the binding energy of the layered bulk material. This strong affinity between the crystal and gold effectively overcomes the interlayer forces, facilitating the separation of individual monolayers during the exfoliation process. The ratio between the two is defined by $R_{\mathrm{LA/IL}}$, ratios exceeding 1 indicating a stronger crystal-gold bond than interlayer attraction. BN (1.07), GeSe$_2$ (1.17), and graphene (1.24) are some examples of materials that in theory should be able to be exfoliated, but do possess a $R_{\mathrm{LA/IL}}$ value close to 1 which makes it exfoliation more challenging.

It is apparent that some crystals bond more strongly to the substrate than others. In the case of graphene, the gold layer merely creates small, temporary imbalances in the electrical charge at the point of contact. There is no significant sharing of electrons between gold and carbon atoms in graphene. On the other hand, materials such as black phosphorus, molybdenum disulfide and ruthenium trichloride form a stronger, covalent bond with gold. Covalent bonds involve the sharing of electrons between atoms. Here, we see a reduction in the negative charge near the atoms at the interface, along with a buildup of charge in the space between them. This indicates a more substantial sharing of electrons between the gold atoms and the phosphorus, sulfur, or chlorine atoms in the respective materials, and thus a stronger bonding.

IV   Kinetic *In Situ* Single-Layer Synthesis

AFTER their discovery in the early 2000s, 2D materials have become one of the most researched materials in the world. While exfoliation techniques have produced 2D materials from certain substances, this approach has limitations, not all materials can be exfoliated and the methods themselves have not seen major advancements for synthesizing 2D materials. These methods primarily rely on mechanical exfoliation using a sticky tape. This method can leave polymeric residue on the surface as well, contaminating the surface. Exfoliation techniques should be improved to increase material yield, substrate adhesion control, lateral size manipulation, as well as contamination minimization to achieve high quality 2D materials, and increase the number of producible 2D materials.

To improve exfoliation the kinetic *in situ* single-layer synthesis exfoliation method was developed. This method presents a new approach to the production of 2D materials, addressing limitations of conventional mechanical exfoliation methods. Ultra-high vacuum, ion sputtering, annealing, extremely flat substrates and cleanliness are used in the KISS exfoliation method to improve crystal quality. To avoid contamination, this process utilizes ultra-high vacuum, which significantly reduces the amount of molecules present that could interact with, and contaminate the substrate, and exfoliation material. This allows for a stronger bond to form between bulk material and substrate during exfoliation, ultimately yielding larger, higher-quality material. Additionally, UHV facilitates *in situ* processing, minimizing contamination risks by keeping the entire process, from cleaning to analysis, within the controlled vacuum environment. Furthermore, preparing a clean and well-structured substrate surface by ion sputtering and thermal annealing is essential for successful KISS exfoliation. Ion sputtering utilizes a focused beam of argon ions directed at the substrate's surface using an electric field. The ions dislodges adsorbed contaminants, efficiently removing surface impurities. However, ion bombardment can also introduce surface defects in the form of vacancies and disrupt the atomic order of the gold film. Thus, this step needs to be followed by thermal annealing. This involves resistive heating a filament close to the sample and letting infrared radiation-anneal the substrate to temperatures close to 340°C in the case of annealing Au(111)/mica. The thermal energy allows the remaining gold atoms on the surface to become mobile. These mobile atoms can then

migrate and preferentially fill in vacancies created during sputtering. This process promotes surface diffusion, ultimately leading to a smoother and more ordered gold surface. The specific parameters of the sputtering and annealing steps, such as ion energy, sputtering duration, and annealing temperature, can be optimized depending on the desired final surface characteristics, making this a versatile technique for surface preparation of various surfaces. The substrate doubles as an exfoliation tool, akin to adhesive tape, and the cleanliness create better adhesion to the surface. Substrate materials such as gold, silver, or germanium can be used for effective substrates.

Three of the main steps in the KISS exfoliation process are shown in *Figure 13*. The first step involves cleaving the bulk material in the vacuum chamber, to expose a contamination free surface. Afterward, the substrate is sputtered and annealed. In the second step, the annealed surface and the bulk material are bought in contact. The forces holding the crystal layers together are often weak van der Waals forces, typically much weaker than the attractive forces between the sputtered crystals and the substrate. These attractive forces can be Van der Waals interactions or even chemical bonds, depending on the materials involved. This difference in attraction forces allows for some of the thin flakes to stay in place on the substrate during the separation process, while the weak bonds between the layers give way.
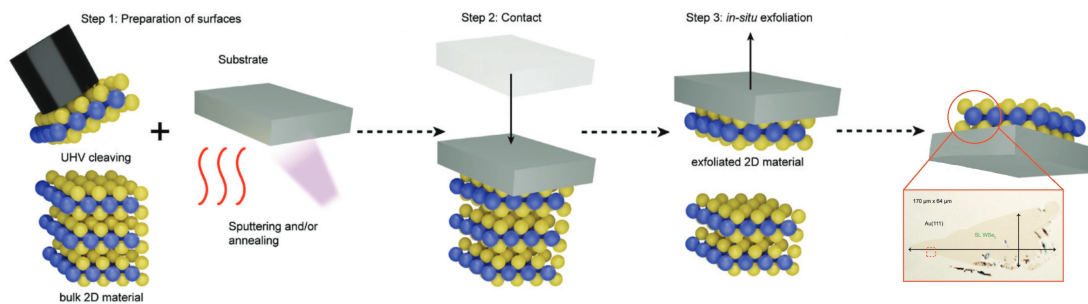
Figure 13: Schematic overview of the KISS exfoliation procedure.[9]

This method was already successful in producing large area single-layer crystals of WSe$_2$ on Ag(111), with an area of 292 µm x 246 µm.[9] An example of KISS exfoliation result is also shown in *Figure 5*, displaying a continuous and homogeneous single layer flake with smaller multi- and bulk layer features. Moreover, LEED data was able to confirm the single domain crystallinity of the exfoliated flake, confirming a 2D material was fabricated. The KISS method was also shown to be successful in creating other two-dimensional materials, emphasizing the universality of the method. The TMDC/substrate combinations WS$_2$/Au(111), WS$_2$/Ge(001) and WTe$_2$/Au(111) were also able to be successfully exfoliated up to a single layered crystal. Additionally, the KISS method extends the production of 2D materials from noble metal to semiconducting substrates. WS$_2$ flakes were successfully transferred onto the (001) surface of germanium, although the flakes appeared smaller with a higher prevalence of multilayer regions compared to those on noble metal substrates. This suggests potential limitations for achieving optimal single-layer coverage on certain semiconducting surfaces using the KISS method.

The short lifetime of air sensitive metallic 2D materials, especially in single-layer form, has also made exfoliation of these materials challenging. Thankfully, KISS exfoliation can be performed in a vacuum, thus eliminating air exposure entirely, effectively circumventing the degradation issue associated with air-sensitive materials. Metallic bulk materials have been studied extensively already and have shown to have interesting properties such as NbSe$_2$ being able to super conduct, the remarkable charge density wave phases of TaSe$_2$, and the Weyl semimetal state observed in WTe$_2$.[20–22] investigating these properties in its single-layer form has been hampered by air sensitivity. Additionally, traditional WTe$_2$ exfoliation techniques typically produce small flakes, hindering comprehensive research efforts. The KISS method overcomes these limitations by enabling the production of large, high-quality flakes of these metals. Many 2D materials, like silicene, germanene, and bismuthene, depend on a substrate for stability, unlike graphene and TMDCs. This dependence makes synthesizing these materials in a 2D form particularly difficult. Previously, CVD and MBE could be used to grow single-layer crystals on the substrate, but KISS exfoliation brings an alternate technique to exfoliate the materials to the substrate that does not require specialized equipment such as source material evaporators.

The success of the KISS exfoliation of various materials has been highlighted, although graphene has yet to be exfoliated using this method, this will be the focus of the second part of this research.

V   Ultra-High Vacuum Systems

$\mathbf{V}$ ACUUM systems that are able to facilitate pressures in the range of 10^{-9} mbar are ultra-high vacuum systems, by definition.[17] A typical vacuum system has a roughing pump, turbo pump and an ion pump, schematics of each pump is shown in *Figure 14*.
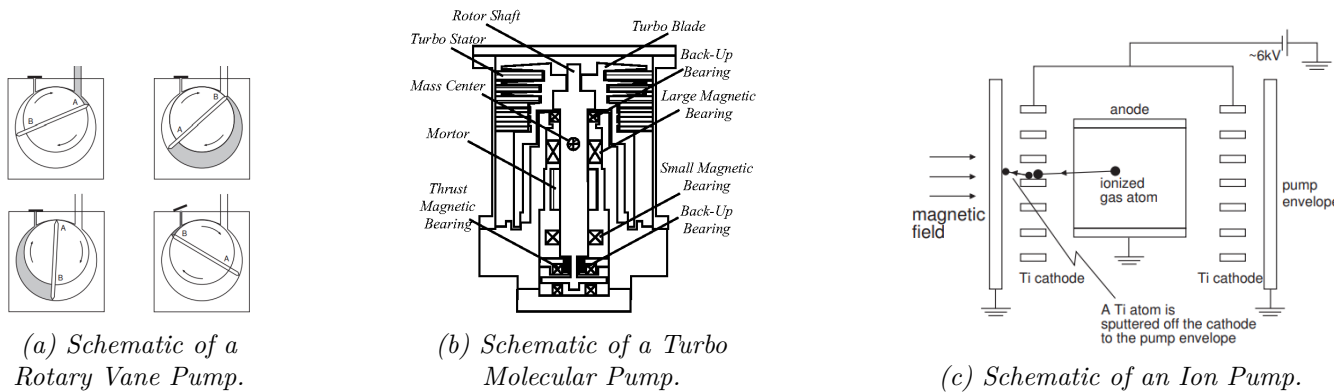

| (a) Schematic of a Rotary Vane Pump. | (b) Schematic of a Turbo Molecular Pump. | (c) Schematic of an Ion Pump. |

Figure 14: Schematic diagrams of various vacuum pumps used in ultra-high vacuum systems.[17,23]

A roughing pump, such as an oil-sealed rotary vane pump, is used to pump the system down to around 10^{-3} mbar, facilitating a pre-vacuum. Another type of pump that can operate in this molecular flow regime is the so-called turbo molecular pump. This turbo pump has a large inlet to its main rotor to increase the chance of molecules entering the pump, and increase the momentum of molecules using high-speed rotating blades. To achieve efficient pumping, the blades of a turbo pump must rotate at very high speeds, typically up to 80,000 rotations per minute. This high speed allows turbo pumps to reach pressures as low as the mid 10^{-10} mbar range. However, it is important to note that this level of vacuum can only be achieved if the roughing pump has already pre-reduced the pressure in the chamber. This is because molecules can back-flow through the turbo pump from the roughing pump, limiting the achievable vacuum level.

The ion pumps is the last pump used in the UHV system. A high voltage discharge within the pump creates a plasma, which is a gas composed of charged particles. This discharge ionizes the residual gas molecules in the chamber, stripping them of electrons and turning them into positively charged ions. The presence of a magnetic field confines these ionized particles, forcing them to travel along a long, spiral path. As the ions travel through the pump, they are attracted to the cathode, which is typically made of titanium. Upon contact with the cathode, the ions can be either absorbed or react chemically with the titanium. Additionally, the high voltage discharge sputters titanium atoms from the cathode, coating the inner surfaces of the pump. This sputtered titanium can further react with gas molecules, enhancing the pumping effect. It is important to remember that ion pumps do not remove gas from the system, they simply transform it into a form that no longer contributes to the overall pressure. Ion pumps can operate across a wide pressure range, typically between 10^{-3} mbar and 10^{-11} mbar. This feature allows ion pumps to be used as a measurement tool to estimate the pressure inside a UHV system. However, operating an ion pump at excessively high pressures can significantly reduce its lifespan. The current drawn by the high voltage power supply of an ion pump is directly proportional to the pressure within the chamber.

There is no single gauge that can effectively span the entire range between atmospheric pressure and UHV. In the initial roughing stage, a Pirani gauge is a suitable choice. It measures the resistance of a heated filament. Collisions with gas molecules cool the filament at higher pressures, but as the pressure drops, collisions become less frequent and the filament heats up. This change in resistance is correlated to pressure and allows the Pirani gauge to operate from atmosphere down to about 10^{-5} mbar. For even lower pressures, an ion gauge takes over. It uses an electron beam to ionize gas molecules, and the resulting ion current is proportional to the pressure. However, the ion gauge has its limitations. Its sensitivity is affected by the gas type, and it has operational constraints at both high and low pressure extremes.
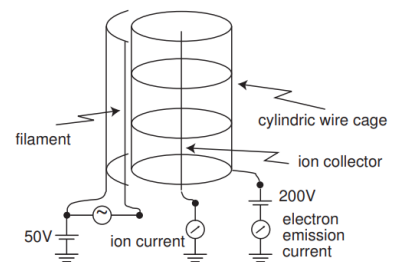

Figure 15: Schematic of an ion gauge.[17]

Materials that make up the vacuum system have to withstand quite extreme conditions. Beyond high-temperature tolerance during bakeout, the material's vapor pressure at operating temperature is equally important. Materials like zinc having a very high vapor pressure even at moderate temperatures, making them unsuitable. Stainless steel is the common choice for chambers due to its low vapor pressure, while tungsten is ideal for filaments in gauges because of its exceptional tolerance. Material properties also have to be taken into account when designing components, such as the KISS bulk holder, that will be brought into the ultra-high vacuum chamber.

VI   Current Holder Design

KISS exfoliation relies on two main components, one being the holder of the bulk material shown on the left side of *Figure 16*, where the bulk material is placed on the head of the bolt. This material is pressed against the substrate that is taped to the pad shown on the right of this figure. The compressive and decompressive motion should be smooth, gradual, and uniform. This is achieved by using a spring locked in between a washer connected to the holder and an M3 bolt head. Both the pad and substrate holder have a small tab that is used to keep them in place or move them if necessary. Detailed technical drawings of the components can be found in *Appendix A*.
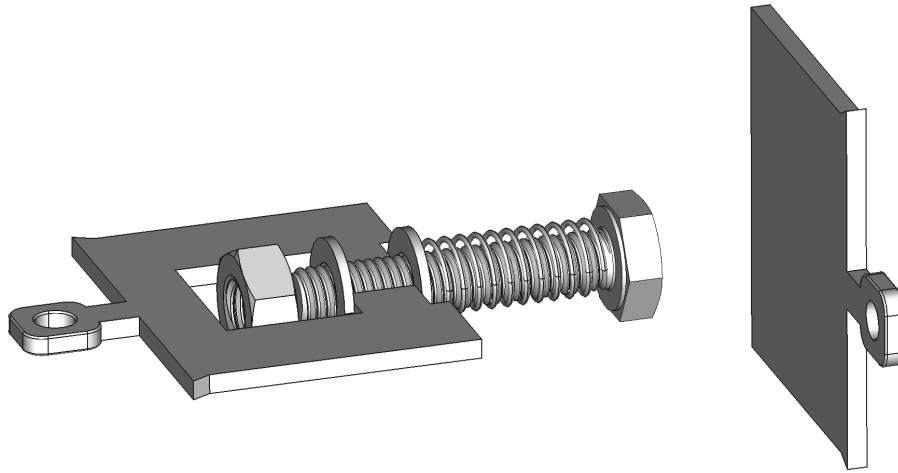
Figure 16: Schematic of the current holder and pad design.

The main problems with the current design are caused by the washers connected to the holder, the robust connection that needs to be made is rather difficult to achieve quickly, as they are welded into place. Even if it is connected, there is still a chance of the connection breaking, ruining measurements. Secondly, the thread on the M3 screw makes compression and decompression unsteady, caused by the thread repeatedly making contact with the washers. Finally, the bolt should only be able to move smoothly in the direction of compression and decompression. This is currently not the case, as there is too much room for it to move in all other directions, even rotate. All of this lowers the chances of good exfoliation results.

Concluding, and drawing from the discussed theory, the research question can be addressed with the formulation of the hypothesis: *Points of weakness in the holder design need to be replaced by strong structures, while also focusing on adjustments that improve uniformity of motion in the direction of exfoliation. Furthermore, UHV KISS exfoliation with sputter-anneal cycles promises cleaner, flatter surfaces and thus better adhesion. Producing larger, higher-quality, and thinner graphene compared to ambient methods.*

III   Setup, Methods & Materials

TWO new bulk material holders were designed in FreeCAD, using a high contrast colors pallet for clarity. The sketches of the designs rely on constraints to bound the holders to their respective shapes. They are designed with a focus on using symmetry constraints to increase adjustability, meaning a change to a

single dimension of an object will not alter its fundamental form. Any holes will stay centered, the pieces remain symmetrical, and all existing connections will remain intact. Technical drawings of each designed were also created using a custom workbench within the program named TechDraw, to give a detailed overview of each holder designed.

A practical method used to exfoliate graphene on a Au(111)/mica substrate is called ambient flame-annealed KISS exfoliation, since all the steps in this process are done under ambient conditions. The holder of the bulk material is shown on the left side of *Figure 16*, and the substrate holder is shown on the right side of this figure. First, a flame is held parallel to the substrate for several seconds, this prepares the substrate for exfoliation. Secondly, graphite is attached to the head of the M3 bolt, the bolt is screwed in place using the nut securing the spring in between. The attached bulk material is cleaved using sticky tape, removing the top layer of the graphite, preparing it for exfoliation. Lastly, the graphene can be exfoliated by compression and decompression of the graphite on the substrate, the motion should be uniform and last only several seconds. The results can be measured using an optical microscope. Exfoliation should be performed multiple times with multiple samples to ensure accurate size and reliability measurements analyzed using the optical microscope.

In the last experiment, all the steps of the graphene exfoliation process are done in ultra-high vacuum, to increase the probability of successful exfoliation. Firstly, the Au(111)/mica substrate should be loaded into the chamber attached to its holder. The substrate then undergoes several cycles of sputtering, annealing, and cooling down. This three-stage cycle takes around half an hour per step. In the first stage, energetic argon ions are fired at the substrate, knocking off and dislodging any contaminants such as dust, oxides, or adsorbed molecules. This creates a clean and pristine surface, essential for good adhesion of the graphene when exfoliating. The second step in this cycle is resistive heating, it raises the temperature of a filament near the substrate to around 340 °C. The heat from the filament then radiates outwards, warming the substrate itself, to decrease stress within the structure and lower surface roughness. Cooling down is the last step in the cycle, which prepares it for another round of sputtering and annealing or exfoliation. Furthermore, the bulk material, in this case graphite, should be facing the substrate in the chamber, while attached to the M3 bolt and locked in its holder with using an M3 nut securing the spring in between. The graphite on top should be cleaved using another sticky tape while inside the chamber, removing the top layer of the material. Afterward, when the materials are setup as described, and according to *Figure 16*, uniform compression and decompression of the bulk material on the substrate should leave graphene residue on the gold substrate, this exfoliation step lasts only several seconds.

LEED characterization of the materials can be done before exfoliation inside the chamber to analyze the gold substrate, but can also determine if exfoliation was effective if it is used after exfoliation. The electron energy of the incident electrons used in the beam should be around 125 eV, at this energy both gold and graphene diffraction spots are well visible. If exfoliation was successful, two sets of six bright dots in the shape of two hexagons will be visible using LEED, with the smaller, brighter hexagon being the reciprocal representation of the gold. The larger hexagon with dimmer and sharper spots show the reciprocal representation of the exfoliated graphene on the surface of the gold. Following this result, optical microscopes can be used to analyze the length and size of graphene crystals exfoliated. Exfoliation should be performed multiple times with multiple samples to ensure accurate size and reliability measurements analyzed using LEED and optical microscopy.

IV   Results

I   New Holder Designs

THE design of the bulk material holder has been changed to make the holder stronger and more user-friendly, by removing the double washer contraption, and replacing it with a solid piece of metal. Moreover, the tolerance of the hole inside this piece was lowered to facilitate a more snug fit with the bolt, decreasing motion perpendicular to the direction of compression. The bolt thread has been shortened, leaving enough space for the nut to tighten on it properly. A smooth motion is ensured by eliminating the possibility of thread catching on the holder walls. The holder is schematically shown in *Figure 17*, with the corresponding technical drawings located in *Appendix B*.
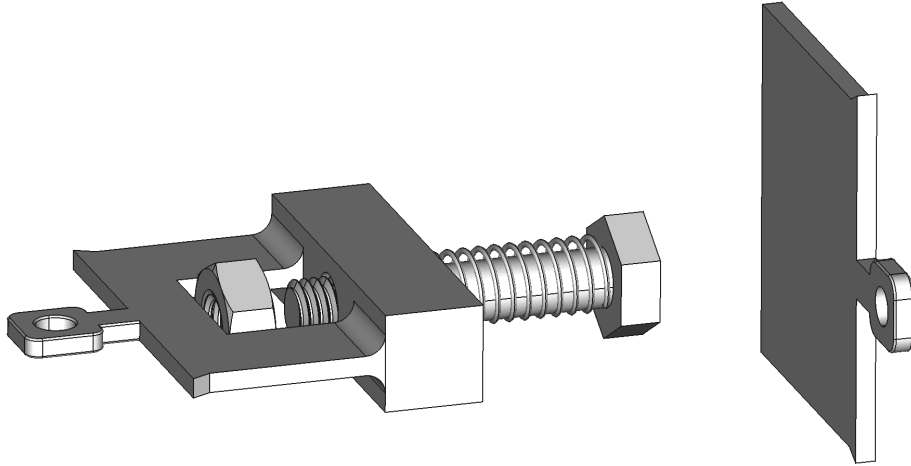
Figure 17: Schematic of an improved holder design, the pad remains unchanged.

Although the previously described holder would suffice in improving exfoliation, rotation of the bulk material on the substrate can still negatively impact results. To mitigate this effect, a design shown in *Figure 18* was developed. It consists of two parts, a press that slides into the holder, and locks in place with a clip. The clip is the substitute for the M3 nut used in previous iterations of the design, and was chosen due to its ease of use and thin design. Giving more room for a structure that improves sturdiness, and only allows motion in the direction of exfoliation, and thus reduce rotation. The importance of exfoliation to occur when pulling normal to the plane, and not exfoliate by shear stress, was also expressed in *Subsection III* of the theory. Where PMMA was more successful in producing single layered graphene than PDMS, because PDMS interacted with graphene through a shearing mechanism which hindered exfoliation effectiveness. Furthermore, the press in the new design substitutes the M3 bolt, allowing for a larger exfoliation area by increasing the size of its head. The main standardized dimension of M3 bolts is its three millimeter diameter and its thread pitch, while other dimensions depend on the manufacturer. Contrary, the newly designed press every dimension is standardized and specifically developed for exfoliation, with the precise dimensions of the structure shown in *Appendix C*.
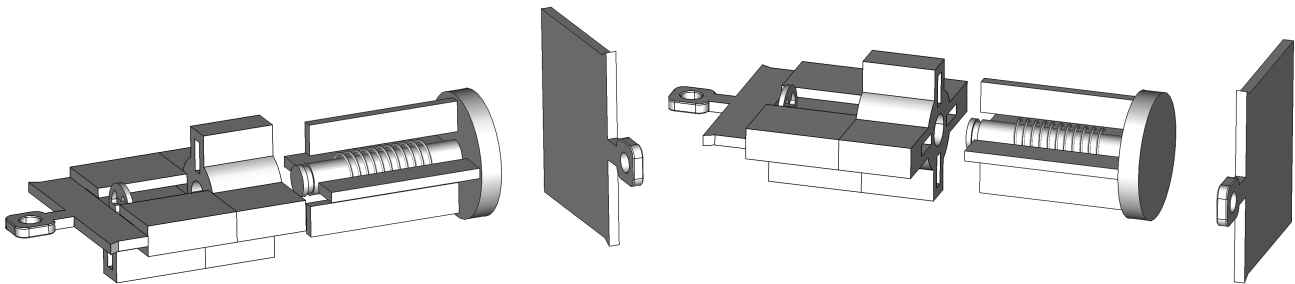

*Figure 18: Two perspectives of a bulk holder design that prevents rotation.*

II   Ambient Graphene KISS Exfoliation

OPTICAL microscope analysis with varying magnifications was performed on three samples of ambient flame-annealed Au(111)/mica with exfoliated graphene. The 6.3x magnification images are omitted from the main text as they do not provide essential details for the analysis, see *Appendix D*. Likewise, imagery documenting the process is found in *Appendix E*. The observed shift from yellow-gold to a darker shade on more magnified samples is the result of the gold substrate's color and magnification. While the base material is inherently yellow-gold, higher magnification restricts light entering the microscope, resulting in a progressively darker appearance. The dark brown flakes on this material are the exfoliated multilayers of graphene. However, this color can also be attributed to contamination of the sample, scratches on the surface, or the bulk material graphite.

The first result is shown in *Figure 19*. Two relatively large multilayer graphene flakes on the Au(111)/mica surface are distinguishable. Note that these are located close to areas with a substantial amount of bulk

material, clearly visible in *Figure 19A*. The two multilayer graphene have been magnified and measured, with the bottom crystal having lengths of $173.13 \pm 0.01\,\mu m$, $121.46 \pm 0.01\,\mu m$, and $170.19 \pm 0.01\,\mu m$ depending on the direction of measurement, and thickness of the crystal measured. The top crystal was measured to be $95.88 \pm 0.01\,\mu m$ in length, and $105.71 \pm 0.01\,\mu m$ measured from another angle. As the crystal seems to possess a lower number of layers compared to its bottom counterpart, area measurement of this crystal was preformed, it was measured to be $5273.03 \pm 0.01\,\mu m^2$.
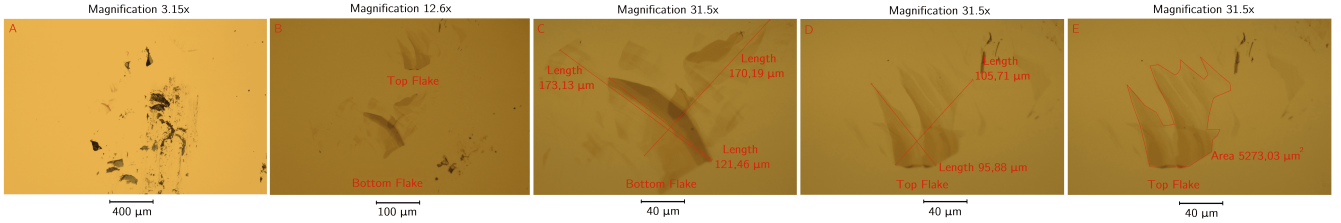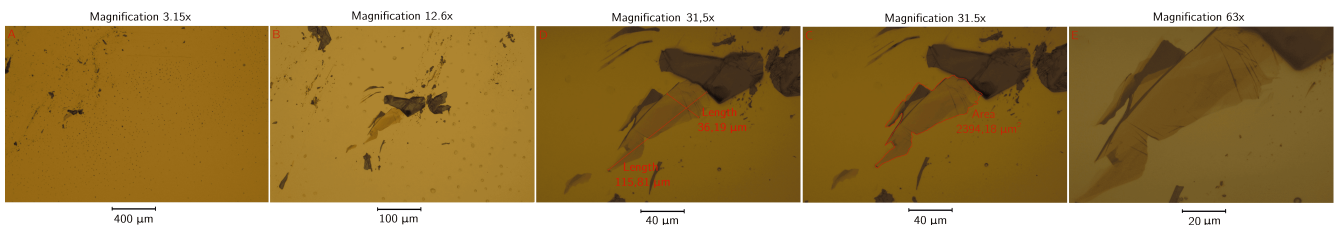

Figure 19: First optical microscope results of ambient graphene KISS exfoliation on flame-annealed Au(111)/mica.

The second exfoliation attempt was less successful, results show a smaller graphene multilayered crystal close to the bulk material in *Figure 20*. While the dark color of this crystal could be due to an increased thickness compared to the others, magnification might also be darkening its appearance. The crystal was measured to be $49.27 \pm 0.01\,\mu m$ long, and $10.30 \pm 0.01\,\mu m$ wide, with an area of $413.15 \pm 0.01\,\mu m^2$.
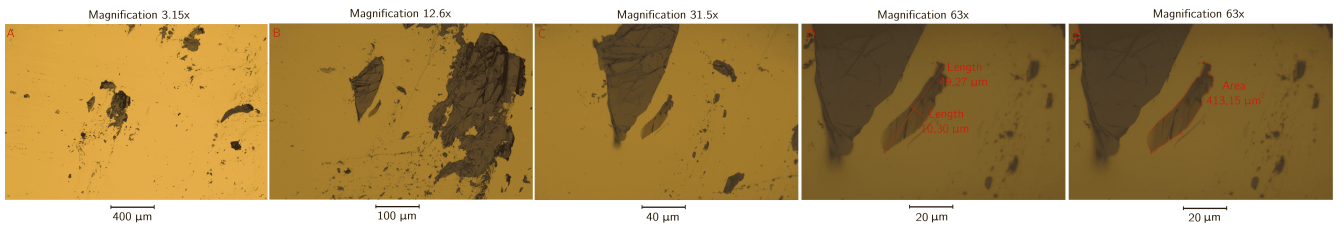
Figure 20: Second optical microscope results of ambient graphene KISS exfoliation on flame-annealed Au(111)/mica.

The results of the third exfoliation attempt show a significant amount of contamination on the images, that expresses itself as dark circular smudges on the sample. Again, the multilayered graphene was located close to the bulk material. With the crystal's length measured to be $36.19 \pm 0.01\,\mu m$ long in one direction, and $115.81 \pm 0.01\,\mu m$ in another. This crystal's area was not directly measured by the microscope's software like the others. Instead, the crystal's area was measured by tracing its outline in the image and using the scale to convert that area to a size of $2394.18 \pm 0.01\,\mu m^2$. Due to the crystal's size exceeding the microscope's field of view at maximum magnification, both measurements were conducted at a lower magnification setting.
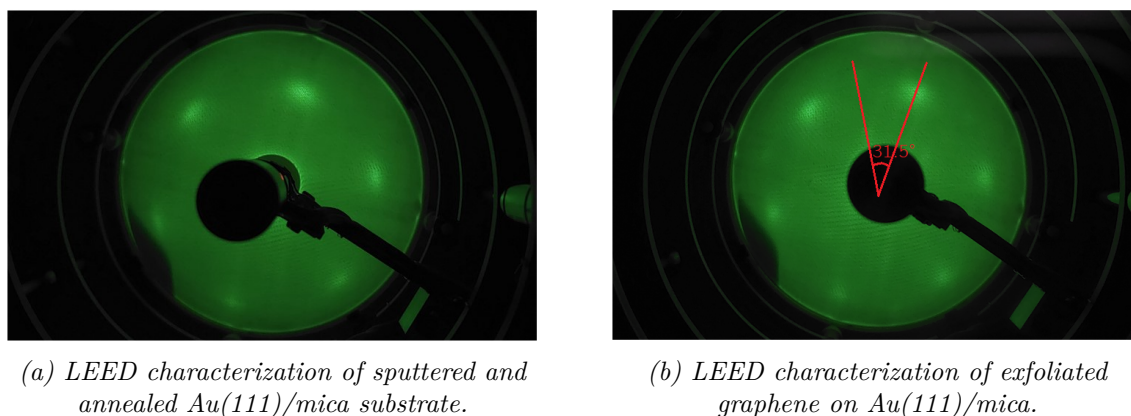

Figure 21: Third optical microscope results of ambient graphene KISS exfoliation on flame-annealed Au(111)/mica.

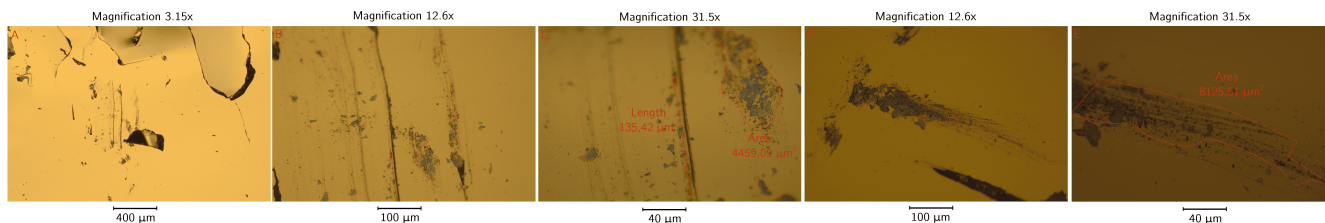## III   UHV Graphene KISS Exfoliation

Under ultra-high vacuum conditions, graphene was exfoliated on a substrate that underwent three sputtering and annealing cycles. LEED was used to determine that exfoliation was indeed successful. The results shown in *Figure 22a* display the LEED pattern of clean Au(111)/mica with its characteristic

six diffraction spots. While *Figure 22b* shows these spots, in addition to six spots coming from exfoliated graphene. The hexagon pattern created by these six small dim dots is slightly larger than the LEED pattern created by the Au(111)/mica. The brightness of the pattern is influenced by the size of the crystal that is analyzed, a smaller crystal will show less bright LEED patterns, meaning this graphene crystal analyzed is relatively small. The substrate is Au(111)/mica, this is a thin film which consists of large gold crystals with a slight misalignment in their crystallographic orientation relative to each other. These large crystals and their misalignment manifests as a bright but wide LEED pattern. Moreover, both gold and graphene have hexagon patterned crystal lattice. The hexagonal arrangement of carbon atoms in graphene's real-space unit cell is also hexagonal in reciprocal space. This manifests as a hexagonal pattern observed in LEED experiments, also shown in the results. Similarly, the face-centered cubic structure of gold projects as a hexagonal pattern in reciprocal space when considering the (111) surface, this was also shown in *Figure 9* of *Subsection II* in the theory. The observations are thus confirmed by theory. Lastly, the orientation of the graphene crystals on the gold substrate was measured to be 31.5°.

(a) LEED characterization of sputtered and annealed Au(111)/mica substrate.

(b) LEED characterization of exfoliated graphene on Au(111)/mica.

Figure 22: LEED characterization of the sample before and after exfoliation, incident electron beam comprised of electrons with a kinetic energy of 125 eV.

Optical microscope measurements show multiple relatively large but thick multilayered graphene crystal groups. One measured showed a $135.42 \pm 0.01\,\mu m$ long strand of seemingly unconnected tiny crystals. Another measurement was done of a group of crystals adjacent to this stand, which had a measured area of $4439.09 \pm 0.01\,\mu m^2$. The last measurement done measured a crystal group to have an area of $8125.51 \pm 0.01\,\mu m^2$. Within each crystal group measured, the crystals could be connected to each other with thinner graphene structures, but these thin layers cannot be identified with certainty on the images generated by the optical microscope. Note that *Figure 23A* shows a large gold flake on top of the sample. This contamination was removed using nitrogen gas, and thus is absent in the subsequent result.

Figure 23: Optical microscope results of ultra-high vacuum graphene KISS exfoliation on sputtered and annealed Au(111)/mica.

V   Discussion

I   Impact of Holder Design Approaches

ALTHOUGH the holder designs developed in FreeCAD are functional, there is still room for improvement. As previously described in the theory *Subsection IV*, effectiveness of exfoliation also depends on the flatness of the substrate and the underlying holder. When redesigning the holder, the materials used did

not change. The metal used is quite rough, which has a possibility of influencing results negatively. A change in materials used could be beneficial, however a cap made of flat polymeric material could also suffice. Moreover, if this cap is sticky, the tape used to hold down the samples could also be disregarded, further negating chances of ridges in the tape and glue negatively impacting results. Simplicity of the designs is also important, which is the focus of the first design. This translates to potentially making the part easier to manufacture, and have fewer parts to malfunction, boosting overall reliability. This is one of the downsides of the second design that focuses more on movement restriction and control. Manufacturing this design will be more challenging, but certainly not impossible. Reliability of exfoliation using this design could increase, however there are parts on the design that could bend which could render it unusable.

In future designs there should be a focus on combining the simplicity of the first design, lowering points of failure, while also keeping in mind the benefits the restriction and careful control of motion the second design gives, improving exfoliation results.

II   Assessing Exfoliation Techniques

THE two exfoliation methods used have both shown promise when exfoliating graphene on Au(111)/mica substrates. The ambient flame-annealed method of KISS exfoliation produced four multilayered graphene crystals with measured lengths and widths of $173.13\pm0.01\,\mu m$ x $170.19\pm0.01\,\mu m$, $95.88\pm0.01\,\mu m$ x $105.71\pm0.01\,\mu m$, $49.27\pm0.01\,\mu m$ x $10.30\pm0.01\,\mu m$, and $115.81\pm0.01\,\mu m$ x $36.19\pm0.01\,\mu m$. Three of these crystals were measured to have areas of $5273.03 \pm 0.01\,\mu m^2$, $413.15 \pm 0.01\,\mu m^2$, and $2394.18 \pm 0.01\,\mu m^2$. One crystal was not measured in area, its thickness was inconsistent.

Exfoliation in UHV showed to produce groups of smaller multilayered graphene crystals with measured areas of $4459.09 \pm 0.01\,\mu m^2$ and $8125.51 \pm 0.01\,\mu m^2$. One measured crystal group was relatively long and thin, with a measured length of $135.42 \pm 0.01\,\mu m$. LEED results of this specific sample also confirmed graphene was indeed exfoliated on the substrate using this method, with its crystal unit cell orientated 31.5° with respect to the gold crystal unit cell, although no preferred orientation of graphene on Au(111)/mica can be extrapolated from this LEED measurement.

Noted that the method of measuring crystal length is not without its flaws, the angle of the measurement greatly affects the value measured. The lack of a standardized method for measuring crystal length due to their diverse shapes and thicknesses renders comparisons between length measurements a less valuable metric to determine exfoliation success. It can also be noted that the substrates exfoliated under ambient conditions showed signs of contamination, while the UHV sample was only contaminated with a gold flake, originating from the substrate, and easily removed with nitrogen gas.

Furthermore, between each exfoliation attempt the graphite was not cleaved again, meaning contamination could have accumulated on its surface in between and during exfoliation attempts, potentially negatively impacting results. This problem could be negated by making sure the bulk material is sufficiently cleaved in between each exfoliation attempt made. The flame used for ambient annealing was held parallel to the surface of the substrate, problems arrise when exfoliating on areas of the substrate the flame did not contact sufficiently. The flame used was quite narrow, in future research, a broader flame should be used to evenly distribute the heat, possibly increasing the reliability of crystal adhesion on the surface. Deviations from the intended UHV exfoliation protocol also occurred, more specifically, graphite cleaving occurring under ambient conditions. This may have led to increased in contamination on the surface of the bulk material compared to the conventional UHV exfoliation procedure. This contamination could potentially hinder the subsequent adhesion of graphene on the substrate. It should also be noted that the substrate in UHV underwent three cycles of ion sputtering and annealing before exfoliation, to clean and restructure the surface. Performing more cycles should be considered in future research to increase the probability of successful exfoliation to take place.

Some measurements using the optical microscope were lower in image clarity and quality, potentially compromising the accuracy of some measurements obtained via optical microscopy. This is caused by the imperfect tuning of the microscope's focal length and illumination prior to data acquisition. Moreover, in some instances the sample did not lay completely flat under the microscope, causing some parts of the measurement to not be completely inside the depth of field of the microscope, and thus out of focus. Making these areas of the sample harder to analyze and measure. In future research, an increase of image

quality should be considered, by adjusting the focal point of the microscope to the correct distance and making sure the samples under the microscope lay completely flat.

While optical microscopy and LEED were used to analyze the results, these techniques alone cannot determine the number of layers the exfoliated graphene crystals consist of. Moreover, LEED was only used to qualitatively measure the exfoliation results. Quantitative LEED measurements should also be considered, which was also discussed in *Subsection II* of the theory. By measuring the I-V curve generated with quantitative LEED and comparing it to theory, information about surface coverage, disturbance, and composition, can supplement the information about the sample already gathered by other methods. In future research, an atomic force microscope should also be used to more accurately determine the performance of both exfoliation techniques. It can precisely measure the height variations of the graphene sheet, determining its thickness and distinguishing between the single-layer and bilayer or thicker forms.

Additionally, AFM generates a detailed image of the surface topography, highlighting wrinkles, folds, or contaminants. This information is crucial for understanding the quality and uniformity of the graphene layer. Finally, angle-resolved photoemission spectroscopy could have also been used in addition to the other microscopes. ARPES quantifies the occupancy of various energy bands, deviations from the ideal band structure observed via ARPES can reveal the presence of defects or impurities in the graphene lattice.

Ultimately, a direct comparison of each crystal area measured was hindered by the variability of the number of graphene layers exfoliated, these variations exist not only between individual crystals, but also within each crystal exfoliated. Determining the optimal exfoliation technique and its efficacy based solely on the size of crystals or crystal groups exfoliated also lacks the necessary nuance needed for this assessment, since there are more variables that determine the quality of an exfoliation method. Lastly, the number of exfoliation attempts made using both methods was too low to accurately assess the efficacy of either method, although the exploratory results show the potential each technique has.

VI   Conclusion

THIS research presented multiple designs of improved bulk material holders used for KISS exfoliation, created using FreeCAD. Holders are designed with clarity, and adjustability in mind by utilizing symmetry constraints. The first design, shown in *Figure 17*, simplifies the original holder by replacing the double washer contraption with a single piece of metal, resulting in a stronger and more user-friendly component, as well as removing redundant bolt threads to increase smooth motion of exfoliation. The second design, shown in *Figure 18*, introduces a holder-press mechanism with multiple protruding pins to restrict rotation of the bulk material, potentially leading to more consistent exfoliation results. While both designs offer advantages, there is room for further improvement. Material selection, particularly for the surface contacting the sample, could be optimized to ensure flatness to minimize negative influences on the exfoliation process.

In conclusion, the trade-off between simplicity and motion control of both designs show the inherent impact of the design choices aimed to improve exfoliation. Where when design prioritizes ease of manufacturing and ease of use, the feature set of the holder decreases. While when design focuses on restricting movement to potentially improve exfoliation results by increasing functionality, the complexity and potential for malfunction increases as well. Showing that, although the hypothesis did give a valid answer to the research question, the complete answer to the research question is more elaborate, by also taking into account design complexity. Future iterations should aim to combine the strengths of both designs.

Furthermore, KISS exfoliation of graphene on Au(111)/mica substrates was performed, with results gathered using an optical microscope in combination with LEED. Exfoliation was performed under ambient conditions using flame annealing, and in UHV using three ion sputtering and annealing cycles to clean and restructure the gold substrate. Both techniques cleaved the bulk graphite before exfoliating.

The experiment aimed to determine the efficacy of exfoliation techniques showed that the ambient flame-annealed method of KISS exfoliation produced multiple multilayered graphene crystals, although some contamination on the samples was visible. Using an optical microscope, four crystals were measured

to have a lengths and widths of $173.13 \pm 0.01\,\mu m$ x $170.19 \pm 0.01\,\mu m$, $95.88 \pm 0.01\,\mu m$ x $105.71 \pm 0.01\,\mu m$, $49.27 \pm 0.01\,\mu m$ x $10.30 \pm 0.01\,\mu m$, and $36.19 \pm 0.01\,\mu m$ x $115.81 \pm 0.01\,\mu m$, which is moderately dependent on the orientation of the measurement. Three of these crystals were measured to have areas of $5273.03 \pm 0.01\,\mu m^2$, $413.15 \pm 0.01\,\mu m^2$, and $2394.18 \pm 0.01\,\mu m^2$. One crystal was inconsistent in thickness, and thus not measured in area.

Conversely, KISS exfoliation of graphene in UHV after radiation annealing and sputtering the substrate in cycles did not produce any large area graphene crystals, it did however produce groups of tiny multilayered crystal structures on the surface of a clean substrate. Two individual crystal groups were measured using an optical microscope and found to have areas of $4459.09 \pm 0.01\,\mu m^2$ and $8125.51 \pm 0.01\,\mu m^2$ respectively. Additionally, a separate thin group of graphene crystals was measured to have a length of $135.42 \pm 0.01\,\mu m$. The success of this exfoliation method was also confirmed with qualitative LEED characterization, which identified a pattern consistent with graphene. Using LEED, the orientation of the graphene crystal with respect to the Au(111)/mica was determined to be $31.5°$. However, one measurement this is not enough to determine the preferred orientation position.

In conclusion, a direct comparison of efficacy based on crystal size is not possible due to the inherent variations in crystal quality, quantity, thickness, and shape obtained during each exfoliation attempt. It is apparent that the use of sputtering and annealing before exfoliation while in UHV showed a decrease in sample contamination, this does point to this process being the superior exfoliation method. While the results offer promising insights, the limited number of exfoliation trials necessitates caution when coming to a definite conclusion. This constraint restricts the ability to confirm or refute the hypothesis.

References

[1] Andre K. Geim and Konstantin S. Novoselov. "The rise of graphene". In: *Nat. Mater.* 6 (Mar. 2007), pp. 183–191. ISSN: 1476-4660. DOI: 10.1038/nmat1849.

[2] Erik Huss. *The Nobel Prize in Physics 2010.* Oct. 2010. URL: https://www.nobelprize.org/prizes/physics/2010/press-release.

[3] Meryl D. Stoller et al. "Graphene-Based Ultracapacitors". In: *Nano Lett.* 8.10 (Oct. 2008), pp. 3498–3502. ISSN: 1530-6984. DOI: 10.1021/nl802558y.

[4] Nathan O. Weiss et al. "Graphene: An Emerging Electronic Material". In: *Adv. Mater.* 24.43 (Nov. 2012), pp. 5782–5825. ISSN: 0935-9648. DOI: 10.1002/adma.201201482.

[5] Changgu Lee et al. "Measurement of the Elastic Properties and Intrinsic Strength of Monolayer Graphene". In: *Science* 321.5887 (July 2008), pp. 385–388. ISSN: 0036-8075. DOI: 10.1126/science.1157996.

[6] Shixiang Yu et al. "Graphene-based lithium-ion battery anode materials manufactured by mechanochemical ball milling process: A review and perspective". In: *Composites Part B: Engineering* 246 (2022), p. 110232. ISSN: 1359-8368. DOI: https://doi.org/10.1016/j.compositesb.2022.110232.

[7] Adrien Mery et al. "Toward the Improvement of Silicon-Based Composite Electrodes via an In-Situ Si@C-Graphene Composite Synthesis for Li-Ion Battery Applications". In: *Materials* 16.6 (Mar. 2023), p. 2451. ISSN: 1996-1944. DOI: 10.3390/ma16062451.

[8] Hojjat Sarvari, Rahim Ghayour, and Esmaeil Dastjerdy. "Frequency analysis of graphene nanoribbon FET by Non-Equilibrium Green's Function in mode space". In: *Physica E: Low-dimensional Systems and Nanostructures v43 n8 (2011): 1509-1513* (2024). ISSN: 1386-9477. DOI: 10.1016/j.physe.2011.04.018.

[9] Antonija Grubišić-Čabo et al. "In Situ Exfoliation Method of Large-Area 2D Materials". In: *Adv. Sci.* 10.22 (2023), p. 2301243. ISSN: 2198-3844. DOI: 10.1002/advs.202301243.

[10] Na Li et al. "Flexible graphene-based lithium ion batteries with ultrafast charge and discharge rates". In: *Proc. Natl. Acad. Sci. U.S.A.* 109.43 (Oct. 2012), p. 17360. DOI: 10.1073/pnas.1210072109.

[11] Jin-Ho Lee, Soo-Jeong Park, and Jeong-Woo Choi. "Electrical Property of Graphene and Its Application to Electrochemical Biosensing". In: *Nanomaterials* 9.2 (Feb. 2019), p. 297. ISSN: 2079-4991. DOI: 10.3390/nano9020297.

[12] Alexander A. Balandin et al. "Superior Thermal Conductivity of Single-Layer Graphene". In: *Nano Lett.* 8.3 (Mar. 2008), pp. 902–907. ISSN: 1530-6984. DOI: 10.1021/nl0731872.

[13] Shen-Lin Chang et al. "Geometric, magnetic and electronic properties of folded graphene nanoribbons". In: *RSC Advances v6 n69 (July 08 2016): 64852-64860* (2016). DOI: 10.1039/c6ra08372b.

[14] Yifan Li et al. "Multiple helical configuration and quantity threshold of graphene nanoribbons inside a single-walled carbon nanotube". In: *Sci. Rep.* 5.13741 (Sept. 2015), pp. 1–10. ISSN: 2045-2322. DOI: 10.1038/srep13741.

[15] Iuliana Mihalache et al. "Engineering Graphene Quantum Dots for Enhanced Ultraviolet and Visible Light p-Si Nanowire-Based Photodetector". In: *ACS Appl. Mater. Interfaces* 9.34 (Aug. 2017). ISSN: 1944-8244. DOI: 10.1021/acsami.7b07667.

[16] Joan Petersen and Susan McLaughli. "3.1: Introduction to the Microscope". In: *Biology LibreTexts* (May 2021).

[17] Philip Hofmann. *Surface Physics, An Introduction.* ISBN 978-87-996090-1-7: Self-Published, 2013.

[18] Robert C. Sinclair, James L. Suter, and Peter V. Coveney. "Micromechanical exfoliation of graphene on the atomistic scale". In: *Phys. Chem. Chem. Phys.* 21.10 (Mar. 2019), pp. 5716–5722. ISSN: 1463-9076. DOI: 10.1039/C8CP07796G.

[19] Yuan Huang et al. "Universal mechanical exfoliation of large-area 2D crystals". In: *Nat. Commun.* 11.2453 (May 2020), pp. 1–9. ISSN: 2041-1723. DOI: 10.1038/s41467-020-16266-w.

[20] Tsuyoshi Yokoya et al. "Fermi surface sheet-dependent superconductivity in 2H-NbSe2". In: *Science* 294.5551 (Dec. 2001), pp. 2518–2520. ISSN: 0036-8075. DOI: 10.1126/science.1065068.

[21] Xian L. Wu and Charles M. Lieber. "Hexagonal Domain-Like Charge Density Wave Phase of TaS2 Determined by Scanning Tunneling Microscopy". In: *Science* 243.4899 (Mar. 1989), pp. 1703–1705. ISSN: 0036-8075. DOI: 10.1126/science.243.4899.1703.

[22] Yanmeng Shi et al. "Imaging quantum spin Hall edges in monolayer WTe2". In: *Sci. Adv.* 5.2 (Feb. 2019). ISSN: 2375-2548. DOI: 10.1126/sciadv.aat8799.

[23] Yi-Hua Fan et al. "Adaptive variable structure controller design of turbomolecular pump with active magnetic bearings". In: *IEEE Conference on Industrial Electronics and Applications* (2008), pp. 1060–1065. DOI: 10.1109/ICIEA.2008.4582679.

Appendices

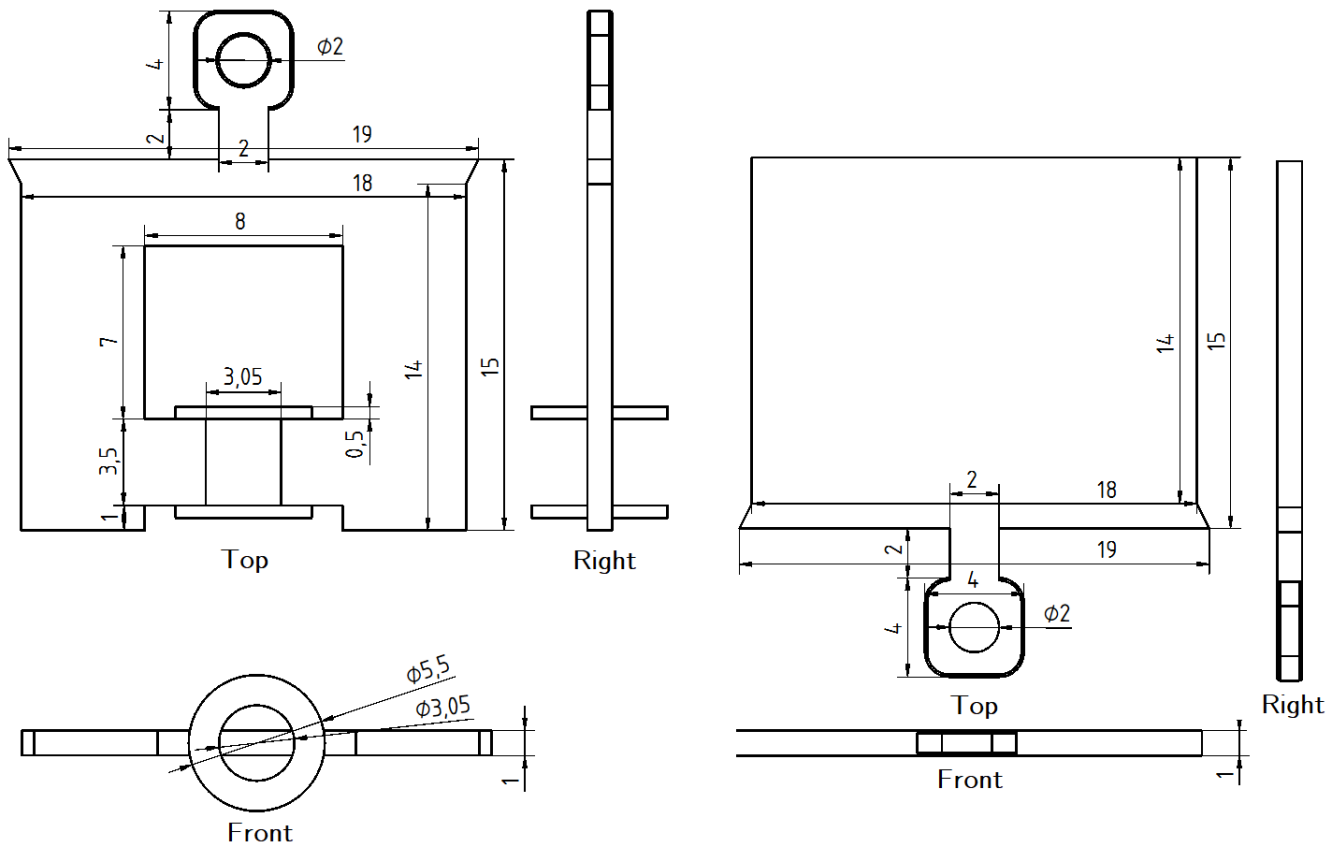## A   Technical Drawings: Current Design

Figure 24: Technical drawing of the current holder bulk holder (left), and substrate holder (right). Units of length are in millimeters.
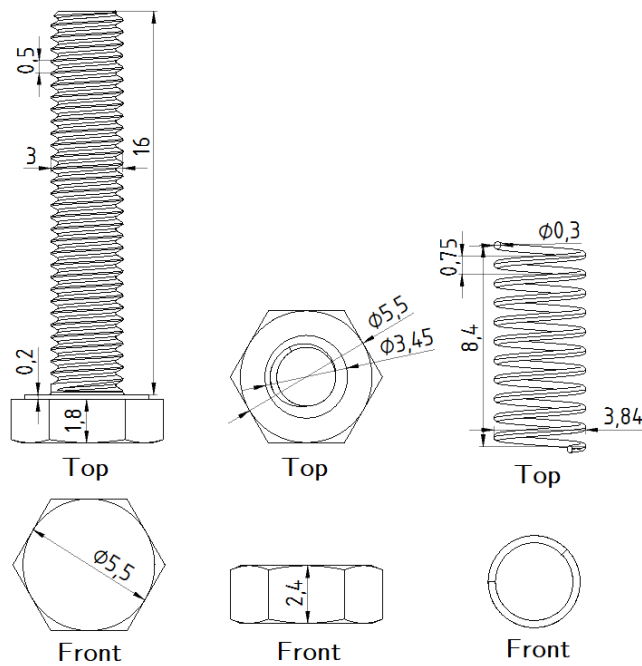

Figure 25: Technical drawing current of bolt, nut, and spring used. Units of length are in millimeters.
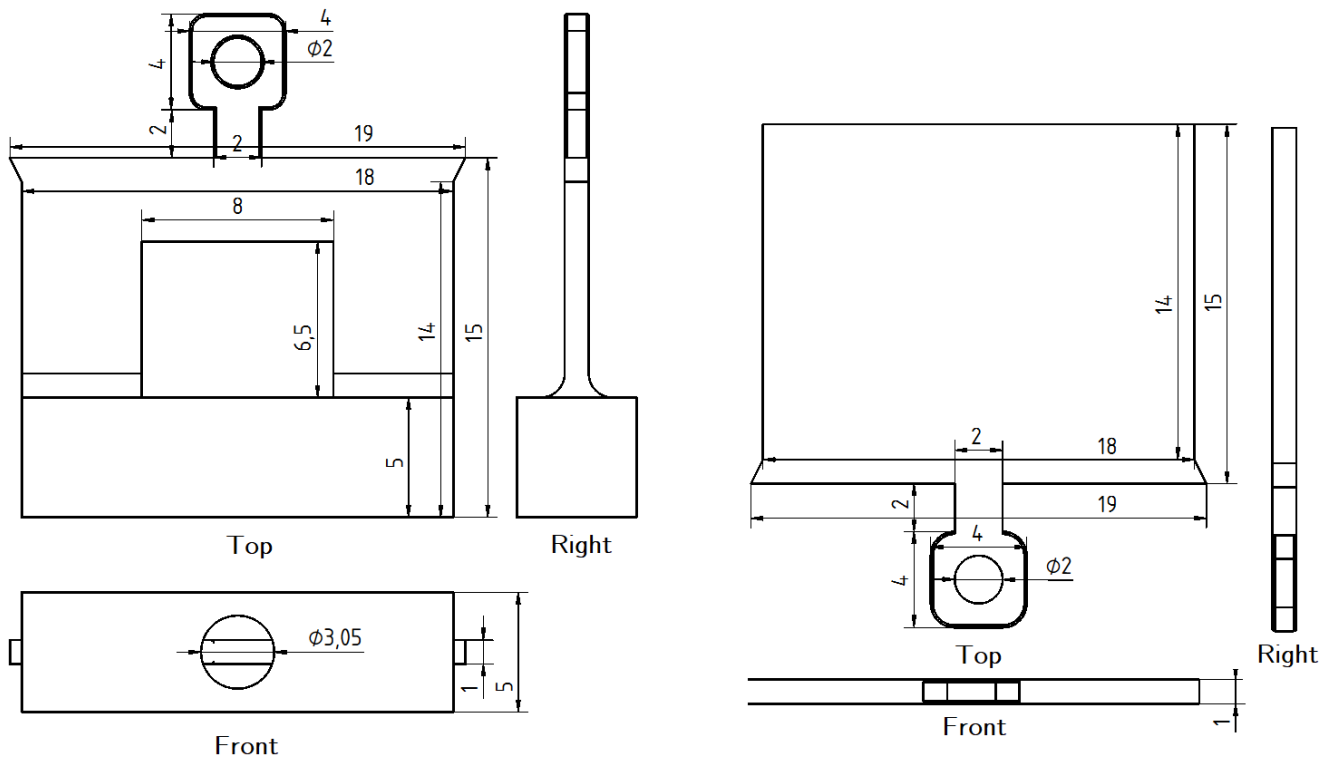
B   Technical Drawings: General Improvements

Figure 26: *Technical drawing of the improved bulk holder (left), and substrate holder (right). Units of length are in millimeters.*
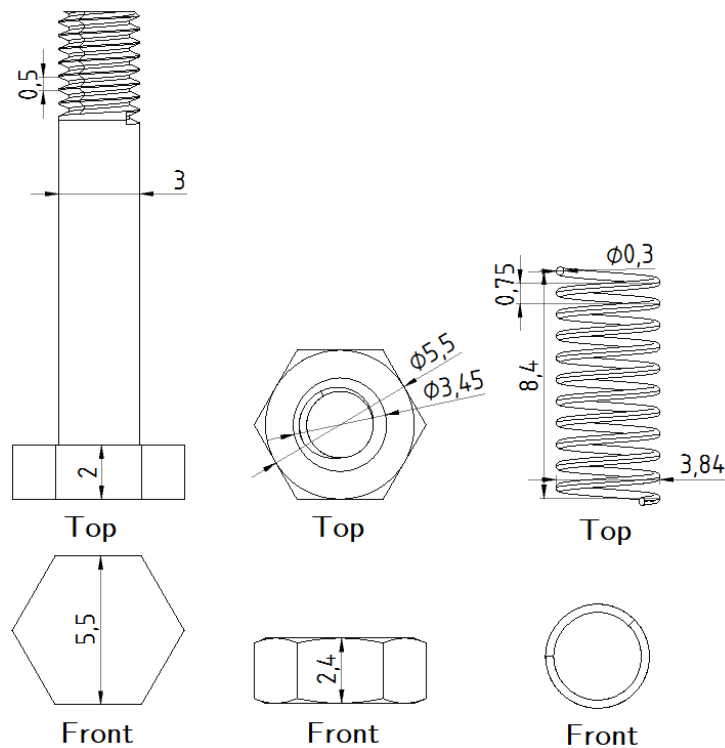

Figure 27: *Technical drawing of the improved bolt, other parts are unchanged. Units of length are in millimeters.*

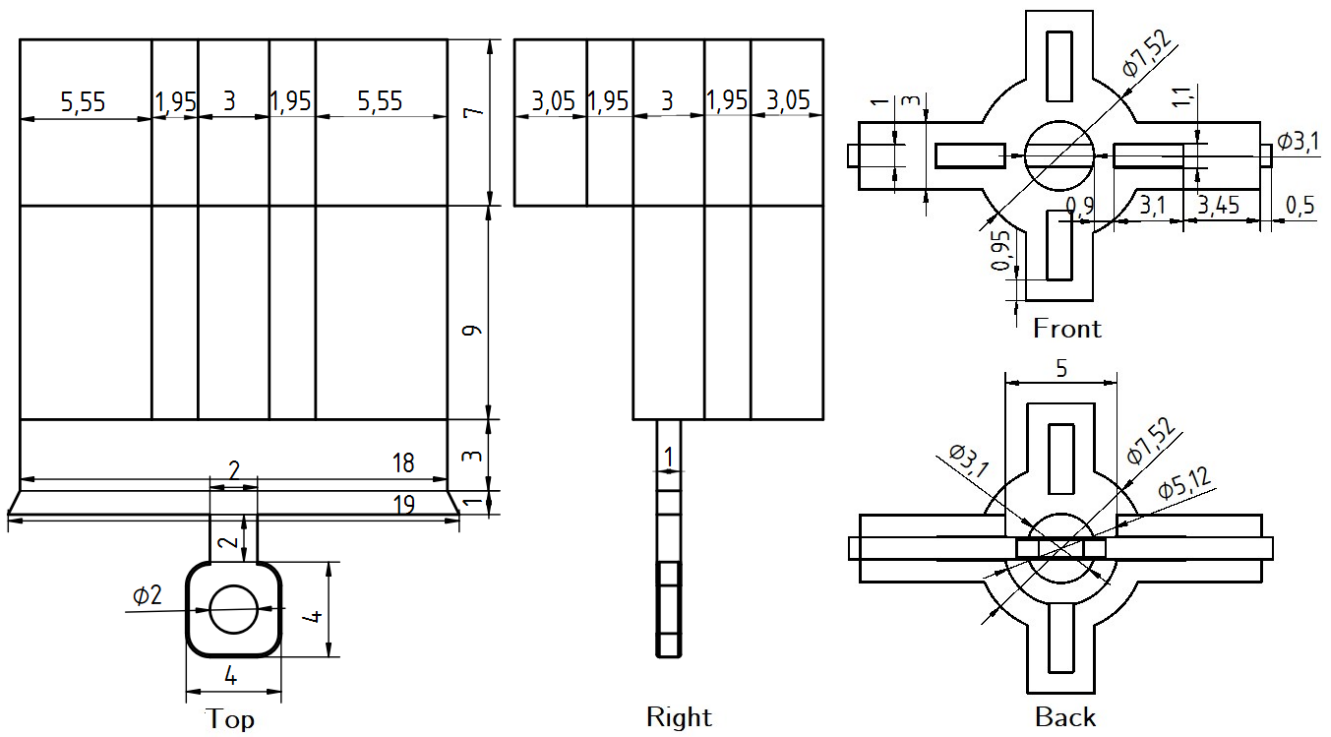## C   Technical Drawings: Restricting Rotation

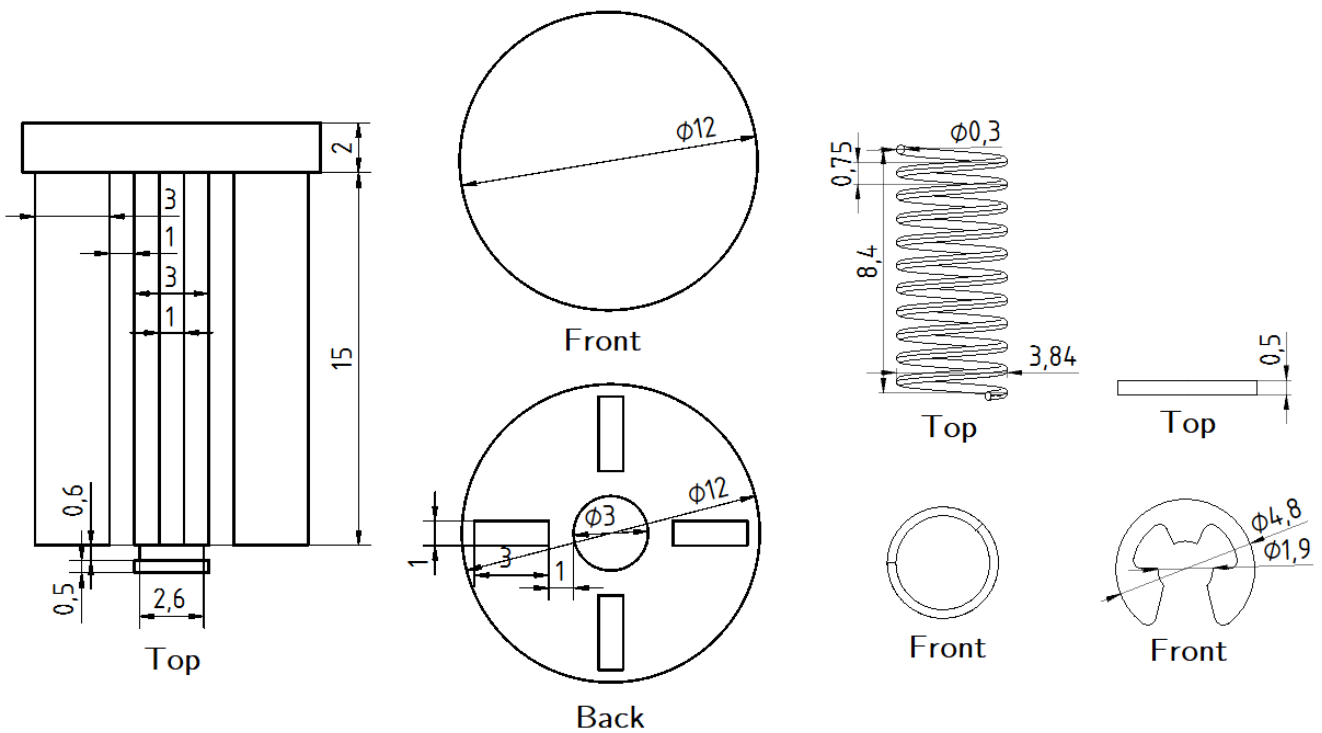Figure 28: *Technical drawing of bulk holder that restricts rotation. Units of length are in millimeters.*

Figure 29: *Technical drawing of the press that slides in the bulk holder, spring, and clip. Units of length are in millimeters.*
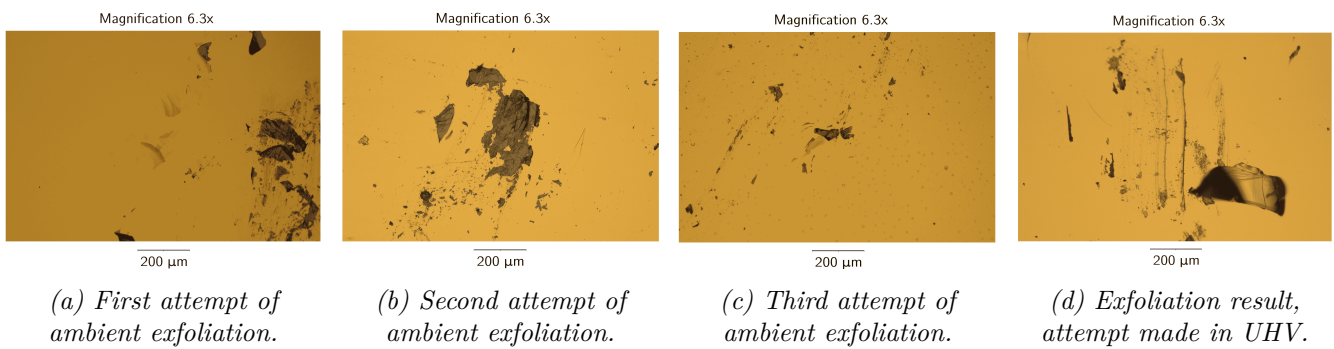
D Supplementary Optical Microscope Results

Magnification 6.3x	Magnification 6.3x	Magnification 6.3x	Magnification 6.3x
200 µm	200 µm	200 µm	200 µm
(a) First attempt of ambient exfoliation.	*(b) Second attempt of ambient exfoliation.*	*(c) Third attempt of ambient exfoliation.*	*(d) Exfoliation result, attempt made in UHV.*

Figure 30: Supplementary optical microscope results of each exfoliation attempt at 6.3x magnification.

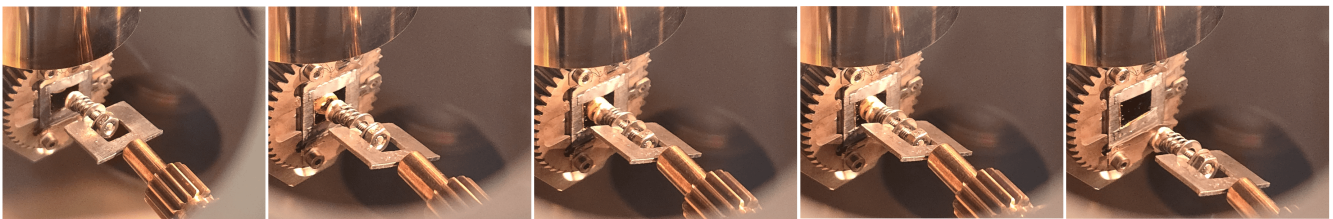## E UHV Exfoliation Process Overview

Figure 31: Photographs of the UHV exfoliation process. The time-lapse shows the initial setup on the left progressing to the completion shown on the right, captured at approximately one second intervals.

university of groningen

faculty of science and engineering